UNIVERSITY OF CALIFORNIA SAN DIEGO

Silicon Photonics for Sensing Applications

A Dissertation submitted in partial satisfaction of the requirements
for the degree Doctor of Philosophy

in

Electrical Engineering (Photonics)

by

Naif Alshamrani

Committee in charge:

Professor Yeshaiahu Fainman, Chair
Professor Prabhakar Bandaru
Professor Ertugrul Cubukcu
Professor Zhaowei Liu
Professor Paul Yu

2022

The Dissertation of Naif Alshamrani is approved, and it is acceptable in quality and form for publication on microfilm and electronically.

University of California San Diego

2022

TABLE OF CONTENTS

LIST OF FIGURES

LIST OF TABLES

ACKNOWLEDGEMENTS

First and foremost, I would like to thank God, whose many blessings have made me who I am today. The work shown in this dissertation is a result of approximately five years of hard work and research. During that time, I had the opportunity to work and collaborate with several individuals in which I am grateful for their support, contribution, and guidance.

I am forever grateful to King Abdulaziz City for Science and Technology (KACST) for given me the opportunity to pursue my Ph.D. degree at the University of California, San Diego (UCSD).

I am also grateful to my advisor and committee chair Prof. Yeshaiahu (Shaya) Fainman for giving me the opportunity to be part of the ultrafast and nanoscale optics group and for his guidance, encouragement, and valuable comments during that time. Joining the group gave me the opportunity to work on several interesting and challenging projects. I would also like to thank my doctoral committee members Prof. Prabhakar Bandaru, Prof. Ertugrul Cubukcu, Prof. Zhaowei Liu, Prof. Paul Yu for their time and valuable comments.

Also, I would like to thank Dr. Andrew Grieco for his fruitful discussions, input, and valuable feedback. I am also thankful to my colleagues, Dhaifallah Almutairi, Andrew Ingram, Jordan Davis, Alex Friedman, Prabhav Gaur, Karl Johnson, Dr. Kim Myun-Sik, and Dr. Ang Li for their collaboration and teamwork during my time in the group.

Moreover, I would like to thank my friends, Sultan Alamri, Abdulelah Habib, Abdurrahman Aljuhani, Mohammad Alsuwaidan, and Saleh Alamri, who were always there when I needed them.

Finally, a special thanks to my parents, wife, son, and siblings, who have given me all the support and love in every step of my life, which eased my academic journey.

Chapter 1, uses information from the white paper “Multifunctional Photonic Biosensors with Information Fusion: Blood Glucose Sensing Application Case”, Andrew Grieco, Naif Alshamrani, Prabhav Gaur, Karl Johnson, and Yeshaiahu Fainman. The dissertation author was a co-author in this manuscript and Yeshaiahu Fainman was the principal investigator. In addition, this chapter uses information from the below manuscripts.

Chapter 2, is in full, a reprint from the manuscript “A Non-Mechanical Multi-Wavelength Integrated Photonic Beam Steering System”, published in Journal of Lightwave Technology, 2021, Naif Alshamrani, Andrew Grieco, Alex Friedman, Karl A. Johnson, Myun-Sik Kim, Francesco Floris, Peter O'brien, and Yeshaiahu Fainman. The dissertation author was the first author in this manuscript and Yeshaiahu Fainman was the principal investigator.

Chapter 3, is in full, a reprint from the manuscript “Miniaturized integrated spectrometer using a silicon ring-grating design”, published in Optics Express, 2021, Naif Alshamrani, Andrew Grieco, Brandon Hong, and Yeshaiahu Fainman. The dissertation author was the first author in this manuscript and Yeshaiahu Fainman was the principal investigator.

Chapter 4, This chapter is in full, a reprint from the manuscript “Side-lobe reduction by cascading Bragg grating filters on a Si-photonic chip”, published in Optics Express, 2022, Sushant Kumar, Naif Alshamrani, Andrew Grieco, and Yeshaiahu Fainman. The dissertation author was a co-first author in this manuscript and Yeshaiahu Fainman was the principal investigator.

Chapter 5, is in full, a reprint from the manuscript “Fabrication-tolerant Fourier transform spectrometer on silicon with broad bandwidth and high resolution”, published in Photonics Research, 2020, Ang Li, Jordan Davis, Andrew Grieco, Naif Alshamrani, and Yeshaiahu Fainman. The dissertation author was a co-author in this manuscript and Yeshaiahu

Fainman was the principal investigator.

Chapter 6, uses information from the white paper “Multifunctional Photonic Biosensors with Information Fusion: Blood Glucose Sensing Application Case”, Andrew Grieco, Naif Alshamrani, Prabhav Gaur, Karl Johnson, and Yeshaiahu Fainman. The dissertation author was a co-author in this manuscript and Yeshaiahu Fainman was the principal investigator.

VITA

2009 Bachelor of Science in Electrical Engineering (Electronics and Communication), King Saud University.

2015 Master of Science in Optical Nanotechnology Engineering, University of Kassel.

2022 Doctor of Philosophy in Electrical Engineering (Photonics), University of California San Diego.

PUBLICATIONS

Prabhav Gaur, Andrew Grieco, **Naif Alshamrani**, Dhaifallah Almutairi, and Yeshaiahu Fainman, "Universal Photonics Tomography," Optics Express 30(11), 19222-19235 (2022).

Sushant Kumar*****, **Naif Alshamrani***, Andrew Grieco, and Yeshaiahu Fainman, "Side-lobe reduction by cascading Bragg grating filters on a Si-photonic chip," Optics Express 30(6), 9983-9991 (2022). (***Co-first authors with equal contribution**)

Naif Alshamrani, Andrew Grieco, Brandon Hong, and Yeshaiahu Fainman, "Miniaturized integrated spectrometer using a silicon ring-grating design," Optics Express 29(10), 15279-15287 (2021).

Naif Alshamrani, Andrew Grieco, Alex Friedman, Karl A. Johnson, Myun-Sik Kim, Francesco Floris, Peter O'brien, and Yeshaiahu Fainman, "A Non-Mechanical Multi-Wavelength Integrated Photonic Beam Steering System," Journal of Lightwave Technology, 39(12), 4201-4208 (2021).

Dhaifallah Almutairi, Alexei Smolyaninov, Andrew Ingram, **Naif Alshamrani**, Andrew Grieco, and Yeshaiahu Fainman, "Vertical-cavity surface-emitting phase shifter," Proc. SPIE 11706, Light-Emitting Devices, Materials, and Applications XXV, 117061T (2021).

Jordan A. Davis, Ang Li, **Naif Alshamrani**, and Yeshaiahu Fainman, "Silicon photonic chip for 16-channel wavelength division (de-)multiplexing in the O-band," Optics Express 28(16), 23620-23627 (2020).

Jordan A. Davis, Ang Li, **Naif Alshamrani**, and Yeshaiahu Fainman, "Novel spectral-shaping building block: a narrowband Mach–Zehnder interferometer," Photonics Research 8(6), 1059-1063 (2020).

Ang Li, Jordan Davis, Andrew Grieco, **Naif Alshamrani**, and Yeshaiahu Fainman, "Fabrication-tolerant Fourier transform spectrometer on silicon with broad bandwidth and high resolution," Photonics Research 8(2), 219-224 (2020).

ABSTRACT OF THE DISSERTATION

Silicon Photonics for Sensing Applications

by

Naif Alshamrani

Doctor of Philosophy in Electrical Engineering (Photonics)

University of California San Diego, 2022

Professor Yeshaiahu Fainman, Chair

Diabetes is an incurable metabolic disease, which has a number of devastating complications if left untreated. It is a leading cause of death worldwide and significantly impacts the live of the patient and their loved ones. Frequent blood glucose measurements must be taken to manage the disease, but conventional meters are invasive, painful, and create a potential avenue for infection. Although significant research effort has been made over the years to introduce and develop less invasive testing devices [Sensors. 19, 1151 (2019)], only one device, which is based on fluorescence technology, was able to obtain the U.S. Food and Drug Administration (FDA) approval (to our knowledge) [Sensors. 21, 6820 (2021)].

The effects that confound the noninvasive sensor stem from the complex measurement environment. The most successful approaches to navigating this sort of complexity involve the combination of multiple complementary spectroscopic techniques in addition to advanced analysis techniques. This combination holds the key to solving the problem of noninvasive blood glucose sensing.

The work shown in this dissertation analyzes different photonic components that can become an adequate candidate for such a system (e.g., a non-mechanical beam steering system, ring grating spectrometer, FTIR spectrometer, and side lobe reduction cascaded Bragg grating filters). While the application of broadband spectroscopy is nearly universal. The cascaded Bragg grating filters shown here can ensure that the spectra of the ring grating spectrometer is partitioned in a very careful way (resulting in sharp skirts). Moreover, the non-mechanical photonic beam steering could assist with optical coherence tomography (OCT). Finally, we propose a multifunctional photonic biosensor with information fusion. The device will leverage recent progress on integrated spectroscopy and fiber sensors to be accurate, portable, inexpensive, and extensible.

Chapter 1

Introduction

Diabetes is a metabolic disease characterized by deficient insulin production or a defective cell response to insulin, which causes abnormal level of blood glucose. Left untreated for long-terms usually results in serious complications such as “atherosclerosis, stroke, neuropathy, nephropathy, and retinopathy” (page 1,[1]). It is a leading cause of death worldwide and significantly impacts the live of the patient and their loved ones. Till this day there is no cure, so frequent blood glucose measurements must be taken to manage the disease and enhance the quality of life. Conventional glucose meters, which are commercially available, employ disposable (single use) testing strips. Such strips require a drop of blood for its measurement; hence the finger-prick/ finger-stick comes into play. This is a source of pain, and breaking the skin creates a potential avenue for infection [1].

Consequently, a significant research effort has been made over the years to develop and introduce a less invasive blood glucose testing devices [1–7]. Some approaches involve the implantation of a subcutaneous glucose sensor which is minimally invasive. However, such devices experience a continuous degradation of sensitivity due to protein accumulation around the sensor, which necessitates frequent calibration. Other approaches seek to be truly noninvasive, and employ various methods of electromagnetic wave glucose sensing, such as spectroscopy or tomography [1]. Despite some promising results, only one device, which is based on fluorescence technology, was able to obtain the U.S. Food and Drug Administration (FDA) approval (to our knowledge) [7].

A successful glucose sensor must meet rigorous requirements for specificity, reliability, stability, sensitivity, and calibration [1,7]. Additionally, environmental factors like pressure, temperature, and motion must be accommodated by the measurement. The failure of the various noninvasive glucose sensors arises from their ability to meet only some of the requirements, but not others. For example, absorption spectroscopy techniques rely on complex calibration methods to achieve the necessary specificity and have a limited penetration depth due to strong optical loss in tissue. In contrast Raman spectroscopy is highly specific but has poor sensitivity. Fluorescence spectroscopy has good specificity and sensitivity, but the measurements are employed on secondary fluids such as tears or sweat, which may lag blood glucose levels [1].

The effects that confound the noninvasive sensor stem from the complex measurement environment (i.e., the presence of many different biological molecules, contaminants, etc.). Currently the most successful approaches to navigating this sort of complexity involve the combination of multiple complementary spectroscopic techniques (i.e., multifunctional spectroscopy) in addition to advanced analysis techniques (i.e., data fusion methodologies). The rich interplay between multiple sensors and data analysis strategies has recently emerged as a key driver for the optimization of production efficiency, quality, and robustness [8,9]. This combination is the key to solving the problem of noninvasive blood glucose sensing.

Finally, tremendous progress has recently been made toward the miniaturization and integration of optical spectrometers, to the point of becoming viable for commercial applications [10]. In the context of multimodal spectroscopy and data fusion this creates a very interesting opportunity. Namely, it should be possible to combine a variety of complementary spectrometers on a single integrated device. Moreover, these sensors will all be driven by a unified microcontroller that can be reconfigured between data analysis strategies based on the desired

application. Such a device would constitute a multifunctional photonic biosensor with information fusion.

In this dissertation we mainly focused on investigating the following novel components, as part of a multifunctional photonic biosensor: a multi-wavelength non-mechanical beam steering system, a high-resolution ring grating spectrometer, a high resolution FTIR spectrometer, and compact cascaded Bragg grating filters that enables high side lobe reduction.

In Chapter 2, we experimentally demonstrate a fully packaged one-dimensional beam steering system that is based on a fully CMOS compatible silicon photonics platform. This configuration enables multi-wavelength operation and is suitable for short-wavelength infrared (SWIR) applications from light detection and ranging (LIDAR) to telecommunication and sensing applications. The switching fabric in this system employs a 1x9 array of add/drop ring resonators that are fed by a common waveguide through a single etch input grating. The switching fabric re-directs the resonance wavelengths at each drop waveguide to the output facet at the edge of the chip and into free space. The divergent beams that exit the waveguides along the output facet are then collimated and magnified using an array of micro-lenses (pitch = 750 μm, Diameter = 700 μm) in addition to a two lens afocal system in order to enhance the fill factor and diminish any blind zones between adjacent beams. Each one of these drop waveguides is used to address portion of the steering aperture. Combined together they enable steering across the entire aperture. Multi-wavelength operation is obtained by placing individual titanium tungsten alloy (TiW) heaters on top of each ring resonator to enable wavelength tuning [11]. This work is in full, a reprint from the manuscript “A Non-Mechanical Multi-Wavelength Integrated Photonic Beam Steering System”, published in Journal of Lightwave Technology, 2021, Naif Alshamrani, Andrew Grieco, Alex Friedman, Karl A. Johnson, Myun-Sik Kim, Francesco Floris, Peter O'brien, and Yeshaiahu

Fainman [11].

In Chapter 3, we introduce and experimentally demonstrate a miniaturized integrated spectrometer operating over a broad bandwidth in the short-wavelength infrared (SWIR) spectrum that combines an add-drop ring resonator narrow band filter with a distributed Bragg reflector (DBR) based broadband filter realized in a silicon photonic platform. The contra-directional coupling DBR filter in this design consists of a pair of waveguide sidewall gratings that act as a broadband filter (i.e., 3.9 nm). The re-directed beam is then fed into the ring resonator which functions as a narrowband filter (i.e., 0.121 nm). In this scheme the free spectral range (FSR) limitation of the ring resonator is overcome by using the DBR as a filter to isolate a single ring resonance line. The overall design of the spectrometer is further simplified by simultaneously tuning both components through the thermo-optic effect. Moreover, several ring-grating spectrometers cells with different central wavelengths can be stacked in cascade in order to cover a broader spectrum bandwidth. This can be done by centering each unit cell on a different center wavelength such that the maximum range of one-unit cell corresponds to the minimum range of the next unit cell. This configuration enables high spectral resolution over a large spectral bandwidth and high extinction ratio (ER), making it suitable for a wide variety of applications [12]. This work is in full, a reprint from the manuscript “Miniaturized integrated spectrometer using a silicon ring-grating design”, published in Optics Express, 2021, Naif Alshamrani, Andrew Grieco, Brandon Hong, and Yeshaiahu Fainman [12].

In Chapter 4, we present a design and experimental validation of a cascaded contra-directional Bragg-grating coupler with a measured main lobe to side lobe contrast of 12.93dB. This level of performance is achieved in a more compact size as compared to conventional apodized gratings and a similar design philosophy can be used to improve side-lobe reduction in

grating-based mirror design for on-chip lasers and other cavity-based designs as well [13]. This work is in full, a reprint from the manuscript “Side-lobe reduction by cascading Bragg grating filters on a Si-photonic chip”, published in Optics Express, 2022, Sushant Kumar, Naif Alshamrani, Andrew Grieco, and Yeshaiahu Fainman [13].

In Chapter 5, we report an advanced Fourier transform spectrometer (FTS) on silicon with significant improvement compared with our previous demonstration in [Nat. Commun. 9, 665 (2018)]. We retrieve a broadband spectrum (7 THz around 193 THz) with 0.11 THz or sub nm resolution, more than 3 times higher than previously demonstrated [Nat. Commun. 9, 665 (2018)]. Moreover, it effectively solves the issue of fabrication variation in waveguide width, which is a common issue in silicon photonics. The structure is a balanced Mach–Zehnder interferometer with 10 cm long serpentine waveguides. Quasi-continuous optical path difference between the two arms is induced by changing the effective index of one arm using an integrated heater. The serpentine arms utilize wide multi-mode waveguides at the straight sections to reduce propagation loss and narrow single-mode waveguides at the bending sections to keep the footprint compact and avoid modal crosstalk. The reduction of propagation loss leads to higher spectral efficiency, larger dynamic range, and better signal-to-noise ratio. Also, for the first time to our knowledge, we perform a thorough systematic analysis on how the fabrication variation on the waveguide widths can affect its performance. Additionally, we demonstrate that using wide waveguides efficiently leads to a fabrication-tolerant device. This work could further pave the way towards a mature silicon-based FTS operating with both broad bandwidth (over 60 nm) and high resolution suitable for integration with various mobile platforms [14]. This work is in full, a reprint from the manuscript “Fabrication-tolerant Fourier transform spectrometer on silicon with broad bandwidth and high resolution”, published in Photonics Research, 2020, Ang Li, Jordan Davis, Andrew

Grieco, Naif Alshamrani, and Yeshaiahu Fainman [14].

In Chapter 6, we propose a multifunctional photonic biosensor with information fusion. This chapter uses information from the white paper “Multifunctional Photonic Biosensors with Information Fusion: Blood Glucose Sensing Application Case”, Andrew Grieco, Naif Alshamrani, Prabhav Gaur, Karl Johnson, and Yeshaiahu Fainman.

1.1 Acknowledgment

This chapter uses information from the following manuscripts/white paper:

Manuscript “A Non-Mechanical Multi-Wavelength Integrated Photonic Beam Steering System”, published in Journal of Lightwave Technology, 2021, Naif Alshamrani, Andrew Grieco, Alex Friedman, Karl A. Johnson, Myun-Sik Kim, Francesco Floris, Peter O'brien, and Yeshaiahu Fainman. The dissertation author was the first author in this manuscript and Yeshaiahu Fainman was the principal investigator.

Manuscript “Miniaturized integrated spectrometer using a silicon ring-grating design”, published in Optics Express, 2021, Naif Alshamrani, Andrew Grieco, Brandon Hong, and Yeshaiahu Fainman. The dissertation author was the first author in this manuscript and Yeshaiahu Fainman was the principal investigator.

Manuscript “Side-lobe reduction by cascading Bragg grating filters on a Si-photonic chip”, published in Optics Express, 2022, Sushant Kumar, Naif Alshamrani, Andrew Grieco, and Yeshaiahu Fainman. The dissertation author was a co-first author in this manuscript and Yeshaiahu Fainman was the principal investigator.

Manuscript “Fabrication-tolerant Fourier transform spectrometer on silicon with broad bandwidth and high resolution”, published in Photonics Research, 2020, Ang Li, Jordan Davis, Andrew Grieco, Naif Alshamrani, and Yeshaiahu Fainman. The dissertation author was a co-

author in this manuscript and Yeshaiahu Fainman was the principal investigator.

White paper “Multifunctional Photonic Biosensors with Information Fusion: Blood Glucose Sensing Application Case”, Andrew Grieco, Naif Alshamrani, Prabhav Gaur, Karl Johnson, and Yeshaiahu Fainman. The dissertation author was a co-author in this manuscript and Yeshaiahu Fainman was the principal investigator.

Chapter 2

A non-mechanical multi-wavelength integrated photonic beam steering system

2.1 Introduction

There has always been significant interest in optical beam steering and its applications, particularly for light detection and ranging (LIDAR) applications. While the concept of beam steering itself is not new, advancements in high volume CMOS manufacturing provide a unique opportunity to address the demand for the miniaturization and simplification of these typically complex systems. Conventional optical beam steering systems are often large, heavy, and expensive primarily due to the mechanical components and bulky optics that comprise these free-space optical systems. Typically, such aspects cannot be tolerated due to strict limitations on their size, weight, reliability and cost [15–18]. There is a long history of research efforts directed towards mitigating these issues [16–18]. Most recently [19], publications have focused on non-mechanical beam steering systems based on integrating phased arrays [19,20], in which one-dimensional (1D) and two-dimensional (2D) beam steering systems were tailored towards LIDAR applications [21–23]. While phased array systems are an elegant solution for beam steering, the required emitter spacing scales with operating wavelength. Compared to existing radio frequency (RF) systems the operating wavelengths and therefore design tolerances of optical systems are on the order of 10,000 times smaller. Practical realization of such devices is sufficiently prohibitive

that a number of alternative techniques have been pursued. One such alternative is to utilize a planar imaging system combined with a uniform array of nanoscale optical emitters in a single focal plane [24–26]. Compared to conventional methods [15] this approach has reduced size and weight, relaxed coherence requirements, potential for broad operational bandwidth, improved robustness, reliability, and superior operating efficiency. The result is an integrated, scalable, compact, non-mechanical broadband beam steering system. Such a design has been either proposed or demonstrated in [24–26]; however, the fill factor, defined by the ratio between the emitted beams coverage area and the area it scans, remain an issue. In order to enhance the fill factor to reach a value of unity or slightly larger, the blind-zones between the adjacent emitters need to be eliminated. One approach is to expand the beams by defocusing the optical emitters causing the beams to diverge and become larger thus eliminating the blind-zones [26]. Moreover, it was noted in Reference [26] that the use of a larger focal length diverging lens could increase the effective range of the beam steering device by partially compensating for the divergence. Nonetheless, the use of a diverging beam for illumination reduces performance due to the following issues: (i) illumination spot size with divergent illumination varies as a function of 3D object/scene depth affecting spatial resolution, and if using multi-beam scanning it will additionally cause crosstalk; (ii) illumination power attenuates strongly with distance from the device, strongly limiting scanning range; (iii) to avoid these effects one could use mechanical adjustment to keep the illumination area constant by tuning the focal distance, but this in turn will slow down the scanning time, cause mechanical instabilities, and be subject to fatigue. An alternative approach presented in this manuscript is to introduce a micro-lens array in the planar imaging system, in which each individual emitting beam fills up a particular micro-lens according to its location, thereby expanding and collimating the beam, enhancing the fill factor. Moreover,

our solution is non-mechanical, requiring no adjustment of the emitter's location in order to enhance the fill factor while maintaining minimally divergent illumination and resolution over a 3D object. Furthermore, it is compatible with planar lenses, such that significant weight reduction is possible. This is analogous to the Rotman lens antenna employed in RF systems [27].

2.2 Concept behind beam steering

The basis of the 1D beam steering system that was demonstrated in this paper is similar to that of the 2D beam steering systems reported in [24–26],where an external planar imaging system consisting of one or more lenses is integrated with a fully packaged silicon photonic chip. The photonic chip itself contains both a 1D switching fabric, which is an array of identical ring resonators, and optical emitters, realized by edge emitting waveguides. The laser source is coupled into the chip through a single-mode bonded fiber on a waveguide grating coupler and is then routed through the switching fabric by a common bus waveguide where the resonant wavelength is coupled to the drop waveguide of each ring resonator and then emitted into free space (see Figure 2.1). The axial position of the individual active (emitting) waveguide with respect to the optical axis of the imaging system (see Figure 2.1) can be controlled by the corresponding individual ring resonator switches. The waveguide output is then mapped by the optical system into the far field as collimated beams to perform scanning function for sensing applications (e.g., LIDAR). The angle of the output beam is determined by the axial position of the active waveguide.

In this work, the imaging system is a combination of a micro-lens array and a collimating lens system (afocal system), in which, the micro-lens array is used to collect and collimate the highly divergent output beams from the drop waveguides. In addition, the micro-lens array is used to enhance the fill factor of the beams, thus diminishing blind zones caused by the distance between neighboring output waveguides. The afocal system is then used to magnify and redirect those

collimated beams into the far field. The transverse location of those collimated beams in the far field is determined by the location of the output waveguides.

Next, we briefly describe the optical system to determine the relation between the optical image in the far field, $U_{\text{image}}(u, v)$ and the initial optical field at the output of lens-let (i.e., micro-lens) array, $U_{\text{initial}}(\xi, \eta)$ [26,28,29]:

$$U_{image}(u,v) = \frac{1}{|M|} U_{initial}\left(\frac{u}{M}, \frac{v}{M}\right) \tag{2.1}$$

$$Magnification(M) = -\frac{f_2}{f_1} \tag{2.2}$$

It is common in scanning systems to consider the angular resolution, $\theta_{\text{resolution}}$ and the scanning angular range, θ_{scanning}, which will depend on the spacing between output waveguides in our system (emitters) and the total number of emitters on the chip, as expressed by [25]:

$$\theta_{resolution} = \tan^{-1}\left(\frac{w_{res}}{f_1}\right) \tag{2.3}$$

$$\theta_{scanning} = \tan^{-1}\left(\frac{w_{scan}}{f_1}\right) \tag{2.4}$$

where f_1 is the focal length of the first Fourier lens, L_1 in Figure 2.1, w_{res} is the distance between adjacent edge emitting waveguides of the chip that is designed to adapt to the micro-lens array parameters (whose pitch = 750 μm, diameter = 700 μm), and w_{scan} is the distance between the farthest waveguides in this design, i.e.,$(N-1)w_{res}$, with N being the number of emitters on a chip yielding N resolvable elements in the far field.

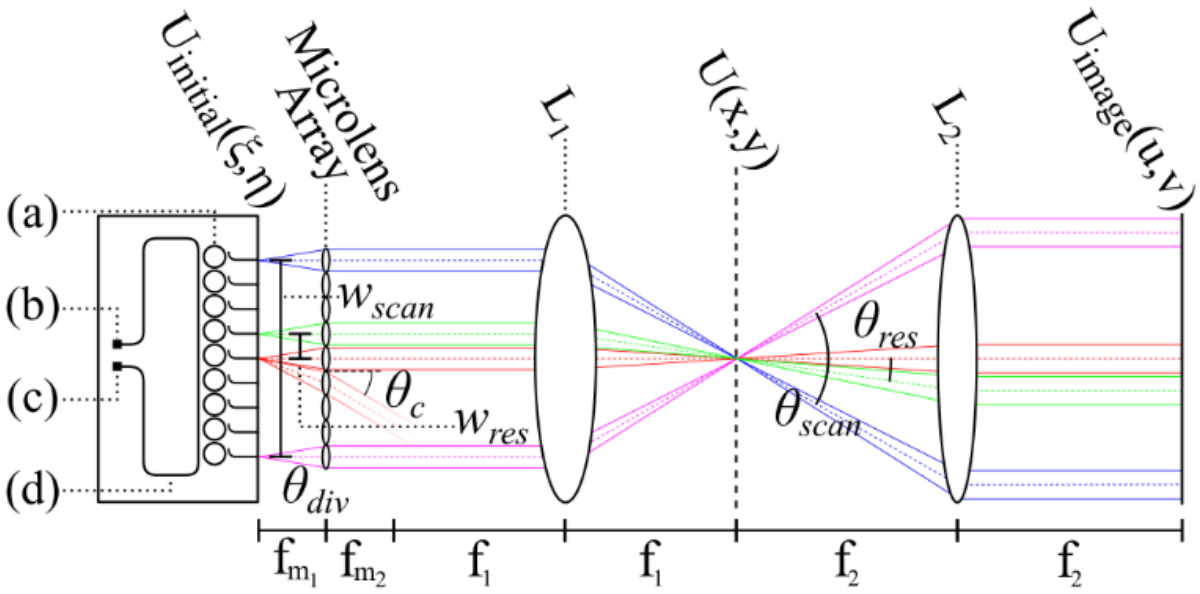

Figure 2.1: Overview of a one-dimensional (1D) integrated photonic beam steering system. The angular resolution and scanning angles are shown to be dependent to the emitter (waveguides) pitch. fm_1 and fm_2 are the back and front focal lengths of the micro-lens array. L_1 and L_2 are the Fourier lenses, U(x,y) and $U_{image}(u,v)$ are the Fourier and image planes, respectively. The photonic chip consists of: (a) Ring resonators, emitters (waveguides), and heaters, (b) Output grating, (c) Input grating, (d) Bus waveguide. The beams propagating from the waveguide emitters and exiting the lens-let array are represented by $U_{initial}$ (ζ,η).

2.3 Device layout and characterization

2.3.1 Silicon-on-insulator photonic chip

The beam steering chip shown in Figure 2.2 was designed and fabricated as part of a multi-project-wafer (MPW) run at the Applied Nanotools foundry [30]. A standard silicon on insulator (SOI) wafer with a 220-nm device layer is employed. The designed structures are patterned into the device layer using a soft mask written by electron beam lithography (EBL) and etched by reactive ion etching (RIE). A 2.2 µm thick silicon dioxide (SiO_2) top cladding layer is then deposited by plasma enhanced chemical vapor deposition (PECVD). Titanium-tungsten alloy (TiW) heaters are then deposited above each individual ring resonator, which allows dynamical tuning of the switching fabric and are routed to contact pads by a titanium-tungsten aluminum bi-layer, a cross section of one such heating element can be seen in Figure 2.3. Finally, the entire

chip is cladded with a 300-nm thick layer of silicon dioxide (SiO_2) in order to prevent metal oxidation, which can occur under the high voltages used to tune the resonant wavelength of each ring resonator.

As illustrated in Figure 2.2, the design consists of a focusing grating coupler that couples the light into a 220-nm tall, 500-nm wide silicon (Si) bus waveguide. This bus waveguide is a common input port and used to couple light into a column of identical ring resonators (1x9) with a 5-µm radius (r). The resonant wavelength of each ring resonator is then coupled to the drop port and emitted into free space while the rest of wavelengths, which are not coupled to any of the resonators, are remaining in the through port and are coupled out of the chip through a focusing grating coupler. The drop ports in this design are approximately spaced by 750 µm to match the pitch of the micro-lens array.

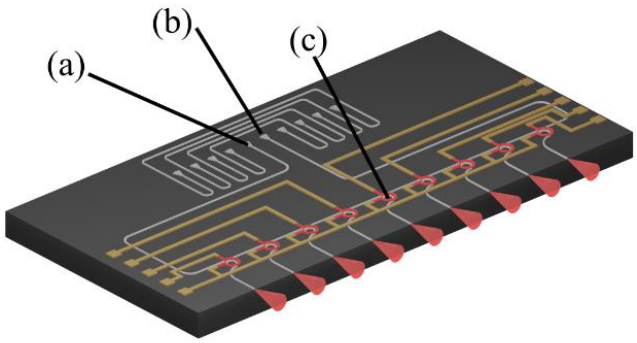

Figure 2.2: One-dimensional (1D) beam steering system composed of: (a) Input and (b) Output couplers, (c) Ring resonator-based switching fabric with integrated heating elements.

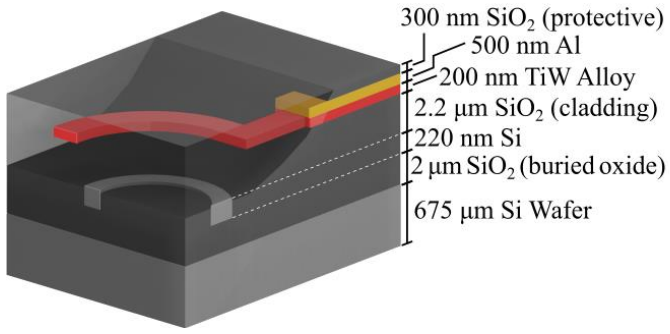

Figure 2.3: Cross section of a ring resonator-based switching fabric in a one-dimensional (1D) beam steering silicon photonic system.

Note that the feed waveguide in our device design is coupled to one or at most few of the ring resonators (for multi-beam scanning), and can be scaled to larger sizes using a branching topology with minimal insertion loss and cross talk. For example, similar Si photonic switching fabrics have been demonstrated that can scale from moderate (i.e., 1024 [31]) to large (i.e., 16,384 [32,33]) number of switches, which is sufficient for practical applications [31–33]. Moreover, with proper design optimization [31,34] it has been shown that such switching fabrics can support insertion loss per drop port of less than 0.5 dB [34] and cross talk of -34 dB [31]. In which, experimental losses per drop port were found to be as low as 0.28 dB [35].

2.3.2 State of the art electrical and optical packaging

This silicon photonics chip was packaged in collaboration with the PIXAPP Pilot Line at Tyndall National Institute. For this reason, the chip needed to be designed to meet the design rules of both Applied Nanotools and Tyndall National Institute. Therefore, the focusing grating couplers used in this design were separated by a 250-µm pitch (center-to-center) to accommodate the pitch of optical fiber bundles. In addition, the farthest grating couplers are reserved for an optical shunt to aid in the active alignment process used for the signal-mode fiber array. A complete listing of design rules and layout tools are reported in other literatures [36,37].

As illustrated in Figure 2.4, the photonic chip is placed at the edge of a printed circuit board (PCB) and is fixed onto a thermistor, which is placed on a thermoelectric cooler (TEC) that is thermally-bonded to the back side of the PCB. This PCB consists of several tracks, which start and end with bond-pads that are wire-bonded to pads on the photonic chip and to serial cable connectors. An active alignment process is applied to align and bond a single-mode fiber array (angle of incidence = 10°) to the chip, in which an index matching epoxy is used to reduce reflections between interfaces. Finally, the entire system is electrically controlled through a ribbon

cable connected to the serial cable connector [36].

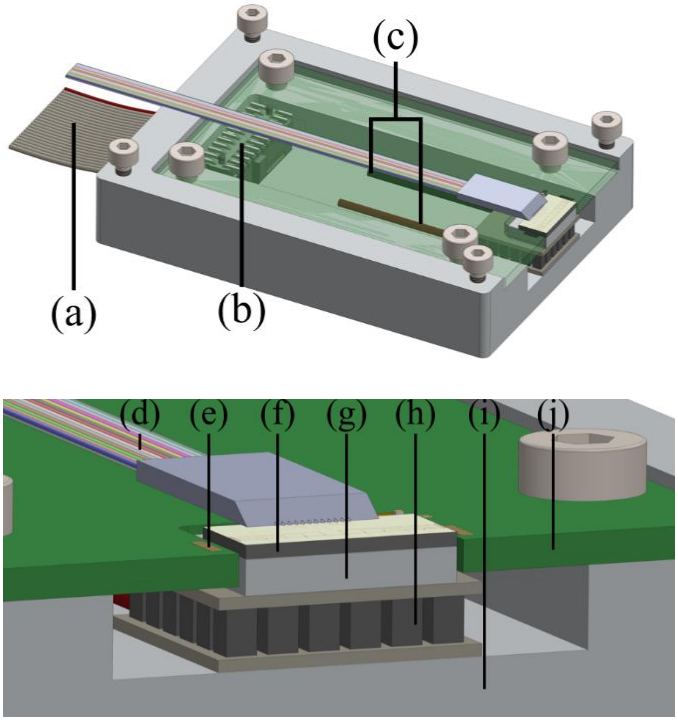

Figure 2.4: Photonics packaging top view (top) and side view (bottom) developed with our PIXAPP partners. (a) Ribbon cable, (b) Serial cable connector, (c) Thermoelectric cooler (TEC) wires, (d) Optical fiber array, (e) Bond-pads, (f) Beam steering chip, (g) Thermistor, (h) Thermoelectric cooler (TEC), (i) Packaging holder, (j) Printed circuit board (PCB).

2.3.3 Experimental setup

A tunable laser (Keysight 81980A/81600B) is coupled to the chip through a polarization maintaining fiber. This is then routed through the switching fabric into waveguides leading off chip by edge termination. The emitted beams pass through an imaging system consisting of a micro-lens array, and an afocal system, from Edmund Optics (49-241 and 49-986). The micro-lens array consists of a column of micro-lenses (1x4) with 750 µm pitch and 700 µm diameter. Each micro-lens has a back and front focal length of 1.3 mm and 1.6 mm, respectively. The collimating lens system (afocal system) is composed of two 9-mm diameter double-convex lenses L_1 and L_2 with focal lengths of 9 mm and 36 mm, respectively (see Figure 2.1). In the far field, an infrared

(IR) camera (FLIR A2600sc) is used to detect and analyze the output field profiles. A power sensor (Keysight -formerly Agilent- 81635A) is used to measure the transmission on the pass-port of the switching fabric thereby identifying the resonant wavelengths for all nine ring resonator as shown in Figure 2.5.

2.4 Experimental results and discussion

2.4.1 Thermal tuning the resonance wavelength

Nine ring resonators of nominally identical path length are used to form the switching fabric of this system. In principle and according to the Lumerical MODE -2.5D varFDTD-simulations all of those ring resonators should have an identical resonance wavelength in the short-wavelength infrared (SWIR) spectrum. However, due to the large spacing between individual ring resonators (i.e., spacing approximately 750 µm), random fabrication variations lead to random changes in the resonant wavelengths as measured in Figure 2.5. Such a variation was anticipated at the design stage, and therefore heaters were employed in order to tune the ring resonators to operate at a common resonant wavelength as illustrated in Figure 2.6.

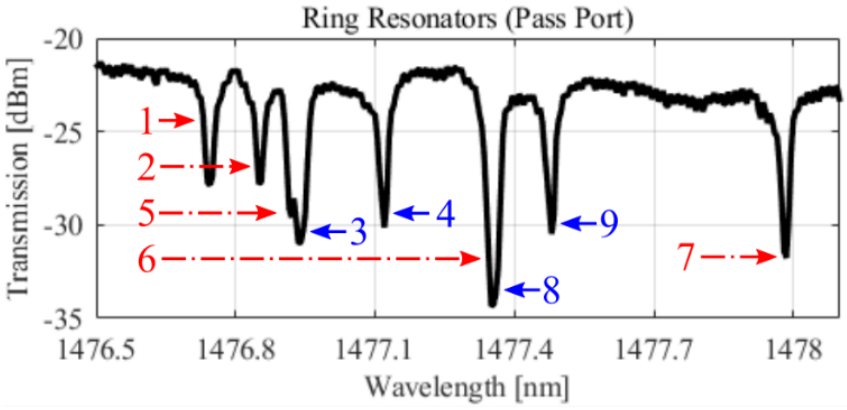

Figure 2.5: Measurement of the transmission spectrum of nine add-drop ring resonators (r=5 µm). The numbers (1 to 9) represent the various resonances for different ring resonators in this design. The measurement took place at room temperature therefore a small wavelength shift occurs compared to Figure 2.6.

Figure 2.5 shows that some resonance peaks have a higher extension ratio (ER) than others.

This effect can be explained by the overlapping of two closely lying resonances (e.g., ring 6 and ring 8) therefore resulting in a higher ER. This was verified by separately tuning the overlapping resonances (see Figure 2.6). The total ER variations are mainly dependent on the spectral variations in coupling efficiency of the input grating.

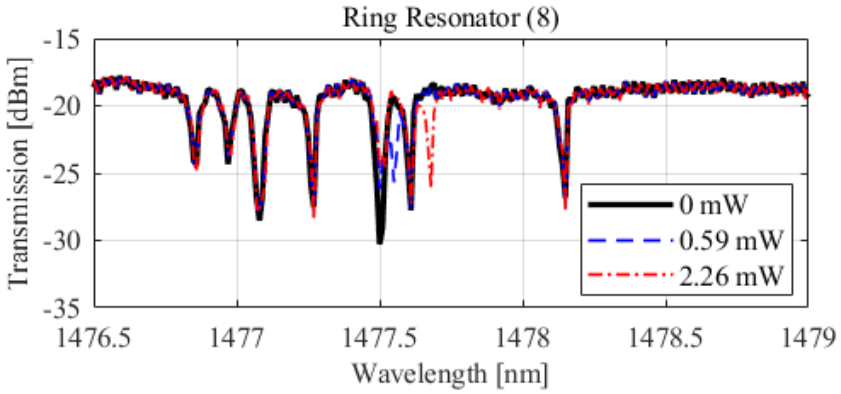

Figure 2.6: Measurement of the transmission spectrum of nine add-drop ring resonators (r=5 µm) while only tuning ring 8. The measurement took place at room temperature therefore a small wavelength shift occurs compared to Figure 2.5.

The thermo-optic effect allows changes in temperature to induce changes in resonant wavelength of the ring resonators through changes in the effective index of the guided mode, see Equation 2.5 [38,39]. Typically, the figure of merit for thermally tune ring resonators is listed in heater power required per nanometer of shift in resonant wavelength. For example, similar thermally tuned ring resonator designs achieve values of 6.19mW/nm [40,41]; however, this metric can be significantly improved by introducing thermal isolation trenches [41]. From the thermal tuning of ring resonator 1 which was measured, we can estimate our $\frac{\Delta P}{\Delta \lambda}$ coefficient to be $\frac{1.47\text{mW}}{0.17\text{nm}} = 8.65\,\frac{\text{mW}}{\text{nm}}$ which can allow us to estimate the required heater power to shift ring 1 to ring 7 (the furthest two resonances) to be $1.29\text{nm} * 8.65\,\frac{\text{mW}}{\text{nm}} = 11.15$ mW. By comparing this to the Applied Nano tools reported average failure power for a 10um radius, 4um wide heater of 344.51mW $\pm$ 50.02mW [42]we see that such a shift is easily achievable. Accordingly, the ring resonator thermo-

optic response may be described as follows:

$$\frac{d\lambda}{dT} = \frac{\lambda}{n_g}\frac{dn_{eff}}{dT} = \frac{\lambda}{n_g}\frac{dn_{eff}}{dn}\frac{dn}{dT} \tag{2.5}$$

where n_{eff} is the effective refractive index, n_g is the group index, and λ is the wavelength. Thermal tuning is an important feature, because it allows mitigation of random fabrication variations, i.e., if the ring resonances could not be fully tuned and detuned to the same wavelength, then there would either be unwanted cross talk in the far-field beam, or blind spots in the scanning range.

2.4.2 Operation without micro-lens

Experimental validation of device performance began by detection the field profiles in the absence of micro-lenses. In this demonstration, the emitting waveguides of the silicon photonic chip are placed at the focal position of the first Fourier transform lens (L_1) in the afocal system. In this configuration, the afocal system offers 4 times of magnification (4x) such that only 2 waveguides can be simultaneously imaged within the field of view of the FLIR camera. Therefore, verification of all outputs requires horizontal translation of either the camera or the experimental device. As shown in Figure 2.7, all the emitting waveguides were alternately tuned to their resonance wavelength and are detected by the FLIR camera.

In Figure 2.7, minor scattering irregularities (e.g., ring 1) can be observed in the transmission of certain waveguides. These arise from imperfections in the diced edge of the photonic chip due to the use of a mechanical dicing tool (Disco Automatic Dicing Saw 3220). This saw based dicing process results in a rough edge facet and thus in a varying degree of scattering. In addition, background noise appears in the center of the chip (e.g., ring 4, 5, and 6). This background noise is most likely from scattering of uncoupled light coming from the input grating couplers, which is centered in the direction of those waveguides as shown in Figure 2.2.

Regardless, the absence of the micro-lenses clearly illustrates the problem of fill factor. The blind zones between adjacent waveguide emitters will impact the beam steering of such a system and influence the fill factor ratio as follows:

$$Fill \quad factor = \frac{N_{spot} \cdot D_s \cdot M}{D_{ST} \cdot M} = 0.001\% \tag{2.6}$$

where N_{spot}, D_s, M, D_{ST} are defined as the total number of emitting waveguides, the waveguide dimeter, the magnification of the afocal system, and the distance between the farthest emitting waveguides, respectively.

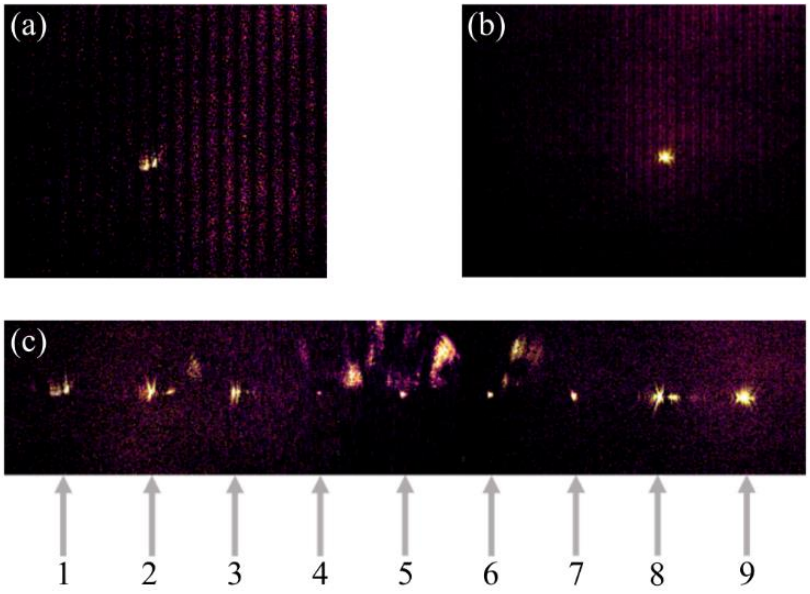

Figure 2.7: Infrared (IR) camera measuring the resonance wavelengths of a 1 by 9 array that is emitting into to free space through the drop waveguides of each ring resonator (without micro-lenses): (a) Ring 1, (b) Ring 9, (c) All 9 rings (composite image).

2.4.3 Blind-zone elimination

In order to enhance the fill factor, the blind-zones between adjacent emitters need to be diminished. One approach is shown in [26], where the optical emitters were defocused from the back focal plane of the first Fourier lens (L1). The intention is to broaden the far field image by

diverging the incoming beam and thereby eliminate the blind-zones. This solution focuses on a single depth plane of interest, which illuminates with a beam that is either converging or diverging. Extending it to other depths would, therefore, require mechanical manipulation to adjust the focal plane, where the beam has minimum spot size. Consequently, the size, weight and power consumption of the total device will be affected. The alternative approach explored in this work employs collimated beams such that no mechanical manipulation is necessary. Additionally, the array of micro-lenses introduced here expand the emitted beams thus enhancing the fill factor by reducing blind-zones as shown in Figure 2.8 and Equation 2.7.

Despite the inclusion of the micro-lenses, the non-uniform light intensity caused by the reflections and the background noise are still observed, but here clearly using micro-lenses as illustrated in Figure 2.8 (e.g., ring 3, 5, and 7), the optical field is expanded to avoid blind-zones in the far field. In order to confirm that the stray light around the center rings arises from unwanted scattering from the grating, ring 5 was turned on and off by tuning the resonance wavelength as shown in Figure 2.9. It clearly shows that the scattered noise only occurs within the proximity of the grating coupler. In future designs the light intensity issue can be avoided by placing the input grating at a different location and designing a more efficient edge coupler with a 1.4 dB loss (fiber to silicon waveguide) [43] in contrast to a 6-7 dB loss in the currently tested device (fiber to silicon grating). Any remaining stray light can be eliminated by introducing silicon pillars in the currently un-patterned space on the chip in order to scatter any undesired noise away from the beam [44–46]. Finally, the beam overlap between adjacent emitting waveguides is a result of inherent inaccuracies in the placement of the micro-lens array at a distance f_{m1} (see Figure 2.1) in the setup.

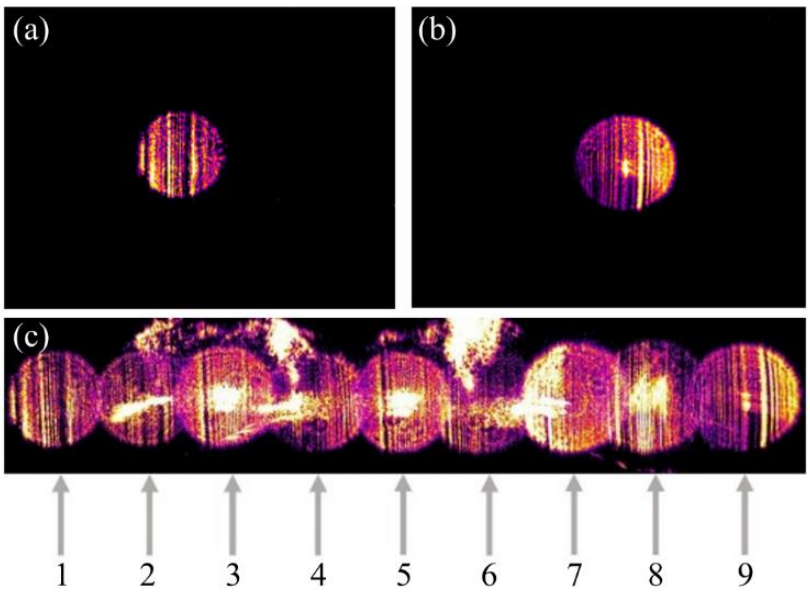

Figure 2.8: Infrared (IR) camera measuring the resonance wavelengths of a 1 by 9 array that is emitting into to free space through the drop waveguides of each ring resonator (with micro-lenses): (a) Ring 1, (b) Ring 9, (c) All 9 rings (composite image).

$$Fill\ \ factor = \frac{N_{lenses} \cdot D_l \cdot M}{\left[\left(N_{lenses} \cdot D_l\right) + \left(\left(N_{lenses} - 1\ \right) \cdot D_{ML}\right)\right] \cdot M} = 94.01\% \tag{2.7}$$

where N_{lenses}, D_l, M, and D_{ML} are the total number of micro-lenses, the micro-lense diameter, the magnification of the afocal system, and the gap between the adjacent micro-lenses, respectively. Finally, by solving Equation 2.3 and Equation 2.4 a scanning angle, or field of view (FOV), of 33.7° and an angular resolution of 4.77° is determined.

According to the Lumerical FDTD simulations, it's important to emphasize that the divergent beams ($\theta_{div(x/2)} \approx 43.5°$ and $\theta_{div(y/2)} \approx 52.8°$) exiting the emitters are leaked into the neighboring micro-lenses (see Figure 2.1). However, those beams are collimated with an angle ($\theta_c \approx 30^o$) thus missing the Fourier lens (L1) of the afocal system. Consequently, no cross talk occurs between adjacent emitters at the image plane. Such a dilemma could be resolved by fabricating the device on a silicon on insulator (SOI) platform with a 3 μm device layer [47] in addition to inverse tapering the waveguide emitters to larger widths thus minimizing the

divergence angle (θ_{div}) in both axes.

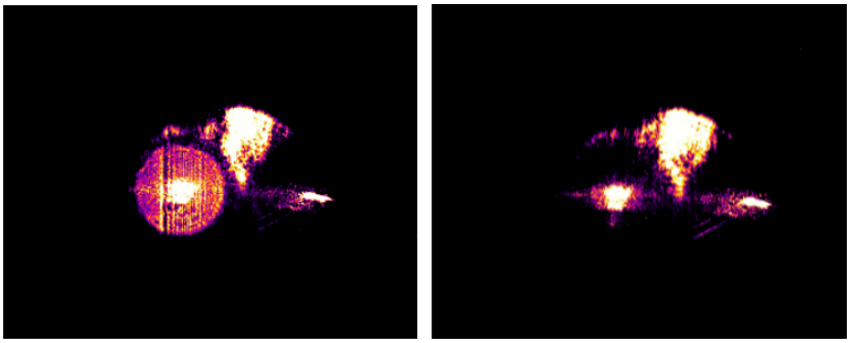

Figure 2.9: Infrared (IR) camera measuring the resonance wavelengths of ring 5 (left) with and (right) without resonance light emitting.

2.5 Future work

The next phase of this work will be to demonstrate a fully integrated 2D beam steering system that offers a much higher packing density [24]. The proposed architecture consists of four discrete functional layers as shown in Figure 2.10(a). The first layer is a planar imaging element that transmits, orients, and collimates beams that are emitted from different locations on the chip. This element could be realized by a single graded index Fresnel zone plate [48], or alternatively a single 2D micro-lens array (commercially available from Axetris down to a pitch of 10 μm and diameter of 9 μm) with an afocal system as shown in this paper. The second layer is a silicon device layer which consists of emitters (e.g., vertical couplers) and a switching fabric (e.g., waveguides and ring resonators). High density vertical couplers can be formed out of plasmonic antennas or angled terminated waveguides [47]. The third layer is an electrical control system layer used to tune the individual heaters placed on the switching fabric. The final layer is an environmental stabilization layer that monitors and compensates for any environmental temperature fluctuations. The approximate size of each layer including the substrate will be on the order of 1mm. Since the emitters occupy the entire plane, arbitrary 2D illumination can be realized (see Figure 2.10(b) for an example of how a single row in a 2-D beam steering system could be

swept across the center plane of the device, full 2-D beam steering can be accomplished by activating other rows).

The design shown in Figure 2.10(a) is highly modular and can be extended to multi-beam operation through the addition of additional stacked device layers. Such a system can be envisioned as a vertical cascade of independently operating narrowband unit cells (see Figure 2.11). This arrangement is possible due to the fact that the diffractive lens system in each layer can be designed to have an additional phase mask that accounts for the unwanted phase modulation induced by the transmission through the subsequent layers in the stack. Such an approach would enable a wider range of bandwidths of operation in which the focal length of the imaging system varies according to the wavelength. From there, as illustrated in Figure 2.11, a set of emitter arrays could be simultaneously operated according to the wavelength and its focal plane. The additional device layers can be composed of any CMOS compatible optical material, such as silicon nitride (Si_3N_4), which is optionally available at most commercial SOI photonics foundry runs, and operates over a broader SWIR window than silicon. The design in this manuscript is simple to extend to other wavelengths, requiring only minor adjustment to the constituent elements such as couplers, switching fabric and micro-lenses. Likewise, the performance should be similar to the experimental performance of the device in this manuscript.

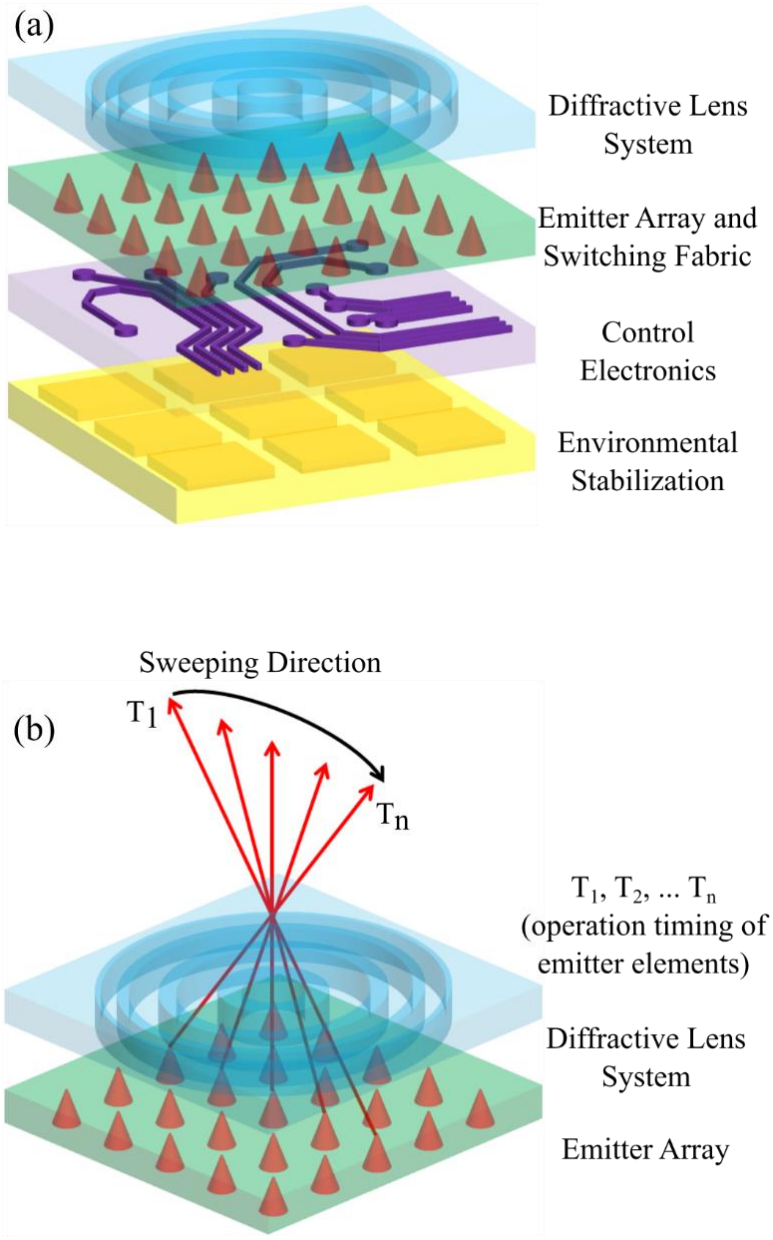

Figure 2.10: Architecture of the beam steering system: (a) Breakdown of the unit cell subsystems. (b) Angular steering is performed by sequential activation of the individual emitter elements. The emitted radiation is collimated in each direction by the diffractive lens system.

Since the switching is performed in a non-mechanically manner, the device lifetime could be comparable to that of integrated CMOS circuitry and the estimated performance of such a system is summarized in Table 2.1.

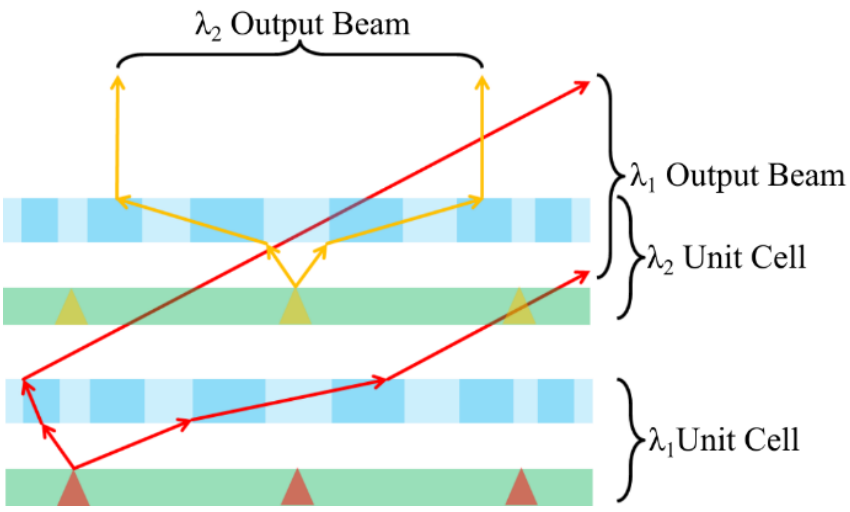

Figure 2.11: Independent stacked unit cells.

Table 2.1: Estimated performance of the 2D beam steering system

Device Parameter	**Estimated Performance**
Switching Time	10 μs
Switching Power	100 μW
Scanning Angle	>120º
Angular Resolution	0.5 º
Bandwidth	Si_3N_4/SiO_2: 300 nm – 3.5 μm Si/SiO_2: 1.2 μm – 5 μm
Maximum CW Beam Power	>20 mW

2.6 Conclusion

In this work we demonstrated a fully integrated 1D beam steering system that operates in the SWIR spectrum in the range of 1476.83 nm - 1478.12 nm. It consists of an external planar imaging system in addition to the silicon photonic switching fabric. The switching fabric was composed of an array of identical ring resonators (1x9), which couple and emit the resonance wavelengths into free space. The scanning angle and angular resolution are directly dependent on the position of the individual waveguide emitters with respect to the optical axis of the imaging system. In addition, a micro-lens array was introduced in the imaging system to enhance the fill factor by reducing the blind zones between adjacent emitters. The system offered a scanning angle

of 33.7° and an angular resolution of 4.77°. Future work can continue to provide further optimization, and yield higher packing densities, even larger fill factors, scanning ranges, and angular resolution.

2.7 Acknowledgment

This chapter is in full, a reprint from the manuscript “A Non-Mechanical Multi-Wavelength Integrated Photonic Beam Steering System”, published in Journal of Lightwave Technology, 2021, Naif Alshamrani, Andrew Grieco, Alex Friedman, Karl A. Johnson, Myun-Sik Kim, Francesco Floris, Peter O'brien, and Yeshaiahu Fainman. The dissertation author was the first author in this manuscript and Yeshaiahu Fainman was the principal investigator. Naif Alshamrani would like to thank King Abdulaziz City for Science and Technology (KACST) for their support during his study.

Chapter 3

Miniaturized integrated spectrometer using a silicon ring-grating design

3.1 Introduction

Spectroscopy is of fundamental importance to scientific disciplines ranging from physics [49] to chemistry [50] and biology [51]. The technological applications are just as vast, including medical research [52], telecommunications [53], and remote sensing [54]. Consequently, a commensurate effort has been made to refine and improve spectrometers [10].

The development of silicon photonics in the telecom NIR bands is a promising avenue for the development of miniaturized spectrometers, overlapping with many chemical absorption bands in the near- and mid-infrared spectral ranges [55,56]. There are many anticipated benefits of photonic integration, including reduced size and weight, reduced noise, increased sensitivity [10,57], simplified environmental stabilization, and reduced power consumption [10]. Finally, the availability of silicon photonics foundries provides a clear path for low-cost commercialization and successful designs.

Recently a variety of integrated spectrometers have been demonstrated [10,57–59]. The most notable designs operate in ways that mimic conventional spectrometer designs employing dispersive optical elements [54,60], as well as several variations based on Fourier transform

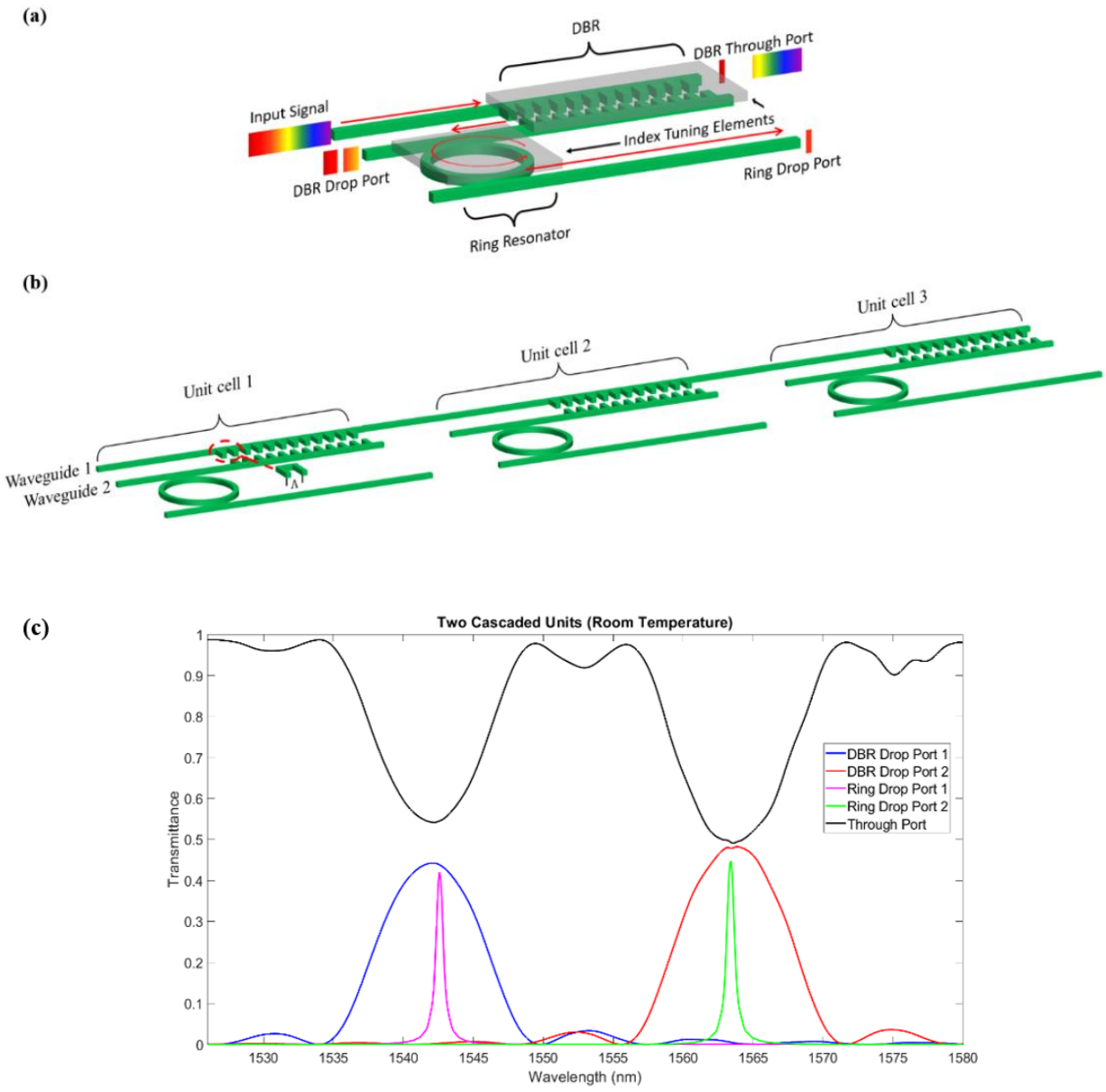

Figure 3.1: Conceptual schematic diagram of the ring-grating integrated spectrometer: (a) Breakdown of a single unit cell (e.g., unit cell 1), where the distributed Bragg reflectors (DBRs) are designed such that the cross coupling band matches that of the ring resonator, thus a segment of the input signal is redirected towards the add-drop ring resonator while the remaining spectra passes through (DBR through port). The ring resonator then acts as narrowband filter hence permitting the resonance wavelength to couple into the ring drop port while the remaining wavelengths propagate towards the DBR drop port (red arrows indicate the path traveled by the optical signal). (b) Several unit cells can be cascaded in order to cover a wider spectral range, where each unit is designed to cover a portion of that spectral. (c) Lumerical MODE - 2.5D varFDTD simulation of two cascaded unit cells with approximately 300 period gratings at different center wavelengths (λ_{c1} = 1542.1 nm and λ_{c2} = 1563.9 nm). For completeness, the self-stop bands outside the operating bandwidth of unit cells one and two are 1588.8 nm and 1610.8 nm, respectively. These stop bands can be pushed further through dispersion engineering that maximizes the difference between n_{eff1} and n_{eff2} according to Equation 3.2 and Equation 3.3.

spectroscopy [57,61]. Nonetheless, the integrated platform introduces unique constraints that pose

a challenge to a direct miniaturization of conventional designs. In particular, the presence of dispersion and thermo-optic nonlinearity in silicon complicates the analysis of Fourier transform based devices, whereas there is much more complexity addressing the high-density integrated detector arrays required by grating based devices.

In this manuscript we introduce and demonstrate an integrated chip-scale spectrometer that has the advantage of being more resistant to thermal drifts. The ring-grating spectrometer presented here is made more resilient through the distributed waveguide Bragg reflector design (DBR) and its large bandwidth which will always match that of the ring resonator even in the event of some drift. The ring-grating spectrometer here is formed by combining a narrow-band filter realized by an add-drop ring resonator with a broadband filter that consists of a distributed waveguide Bragg reflector (DBR) as shown in Figure 3.1 [39,62,63]. Compared to conventional spectrometers, this design realizes a chip-scale spectrometer with high spectral resolution, extinction ratio (ER) and spectral throughput. Moreover, the fabrication process for this spectrometer is compatible with processes available at global CMOS foundries, offering a direct route to cost-effective fabrication. The ER and spectral resolution characteristics of this device are determined by the ring transmission (at drop port) and the Q-factor, respectively. The device shares the advantages of other individually addresses pixel detector designs, in the sense that the gain of the individual pixels can be adjusted for optimal dynamic range. This compares favorably to conventional dispersive spectrometer designs that employ CCD detector arrays. This is due to the gain limit of the detector array is the same across all the pixels. In the common scenario that adjacent pixel's rows are exposed to differences in power density (each row corresponding to a different wavelength), this manifests as a dynamic range limitation. This is because the maximum gain of the lower power pixel rows is limited by the highest power pixel row. Moreover, when

comparing the work shown in this manuscript to a planar echelle grating spectrometer it is clear that the latter one consists of static arrays and the number of detectors required to realize high resolutions will not only result in a larger number of detectors but while also demand a large footprint [10]. In contrast, the ring-grating spectrometer shown here uses the same detector and is capable to tune over reasonable bandwidth (i.e., 30 nm) with the resolution of the ring resonator. Furthermore, the fundamental device unit cell (illustrated in Figure 3.1) can be stacked in series to cover additional spectral bands in support of broad band applications. This can be done by centering each unit cell on a different center wavelength such that the maximum range of one-unit cell corresponds to the minimum range of the next unit cell. This is quite useful in the event that the maximum spectral range provided by the tuning mechanism is smaller than necessary [62]. The thermo-optic effect in both components is essentially identical therefore both elements can be thermally tuned simultaneously hence simplifying the overall design and enabling the capability to shift transfer functions of both filters thus apodization of the Bragg grating is unnecessary [62]. Finally, in comparison to FTS the ring-grating spectrometer shown here can offer sub-nm resolution with a small footprint design while FTS demands huge footprint design (i.e., mm's of waveguide).

3.2 Operating principle of the ring-grating spectrometer

The miniaturized spectrometer shown here (see Figure 3.1) employs a DBR in combination with and an add-drop ring resonator in order to perform a spectral interrogation over the short-wavelength infrared (SWIR) spectrum. The DBR functions as broadband filter and is designed by utilizing the cross-coupling Bragg condition [63]:

$$\beta_1(\lambda_c) + \beta_2(\lambda_c) = \frac{2\pi}{\Lambda} \tag{3.1}$$

where β_1 is the propagation constant of waveguide one (WG_1), β_2 is the propagation constant of waveguide two (WG_2), Λ is the sidewall grating period for both waveguides, λ_c is the center wavelength of the drop band resulting from contra-directional coupling occurring between the two corrugated waveguides. In this design, the center wavelength of the contra-directional coupling in each waveguide is determined by the effective indices (n_1 and n_2) and can be engineered by modifying the width of WG_1, the width of WG_2, and the grating periods (Λ), such that the cross-coupling band of the static Bragg grating centered at λ_c matches that of the ring resonator. The four port DBR configuration also has two backward coupling Bragg conditions (self-stop bands) [63]:

$$2\beta_1(\lambda_1) = \frac{2\pi}{\Lambda} \tag{3.2}$$

$$2\beta_2(\lambda_2) = \frac{2\pi}{\Lambda} \tag{3.3}$$

where λ_1 is the center wavelength of the back-ward coupling (stop band) in WG_1, and λ_2 is the center wavelength of the backward coupling (stop band) in WG_2. When the left and right waveguides have different widths, the propagation constants β_1 and β_2 will be different, and these bands will be centered far above and below the cross-coupling band. Consequently, they will not interfere with the operation of the device. Moreover, it should be noted that for operation with cascaded multiple unit cells all of them will need to be designed to have these self-stop bands outside the operating bandwidth of the spectrometer. The resonant wavelength (λ_{res}) and the free spectral range (FSR) of the add-drop ring resonator filter is determined by the effective indices and the ring size Equation 3.4 and Equation 3.5 [39].

$$\lambda_{res} = \frac{n_{eff} L}{m} \tag{3.4}$$

$$FSR = \frac{\lambda^2}{n_g L} \tag{3.5}$$

where λ_{res} is the resonance wavelength of the add-drop ring resonator, n_{eff} is the effective index of the add-drop ring resonator, n_g is the group index of the add-drop ring resonator, m is the mode order of the resonance wavelength (i.e., m=1, 2 …), and L is the length of single round trip in the ring resonator (defined as $2\pi r$, where r is the radius of the ring).

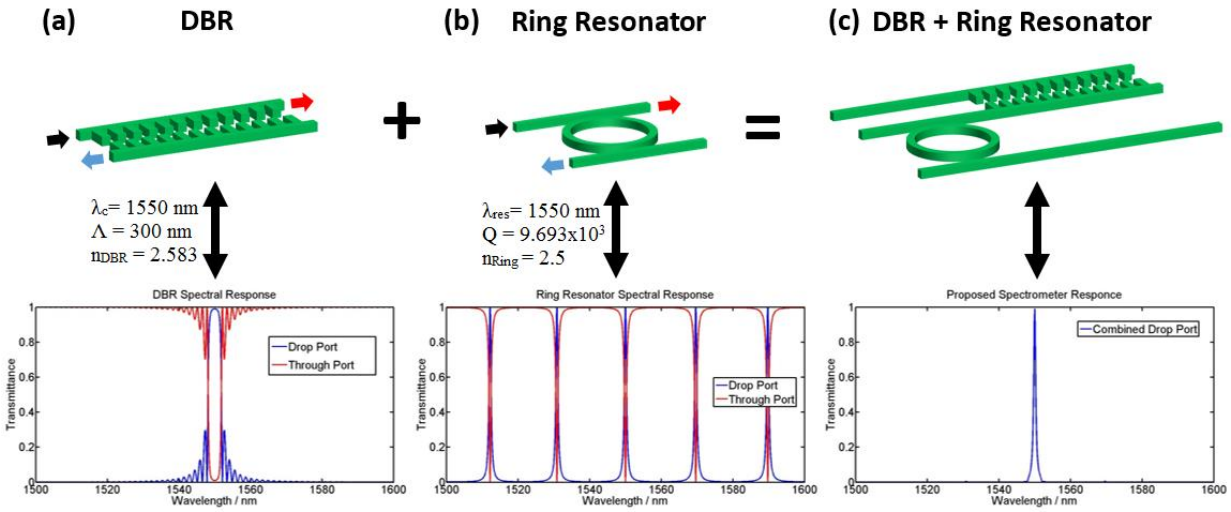

Figure 3.2: Analytical model of the spectral response of an ideal (a) Distributed Bragg reflector (DBR) in which the center wavelength of the contra-directional coupling is at 1550 nm and the effective index of the static Bragg grating is 2.583 (n_{DBR}). (b) Add-drop ring resonator (radius = 5 µm) in which the resonance wavelength is at 1550 nm and the effective index of the ring is 2.5 (n_{Ring}). (c) Distributed Bragg reflector (DBR) and ring resonator (combined).

The overall performance of the DBRs, the add-drop ring resonator, and the DBRs combined with the ring resonator are designed using COMSOL to numerically determine the optical mode parameters of the structure. Through contra-directional coupling, the ideal two waveguide DBRs act as a broadband bandpass filter (λc = 1520 nm) according to Equations (3.1-3.3), while the ideal add-drop ring resonator provides high resolution spectral lines that are spaced according to Equation 3.5. When combining both elements the device behaves as a notch filter thereby isolating a single ring resonance, hence performing spectral interrogation. Figure 3.2 is an analytical model of how a device with the following parameters should ideally perform for λ_c = 1550 nm, Λ = 300 nm, n_{DBR} = 2.583, λ_{res}= 1550 nm, Q-factor = $9.693x10^3$, n_{Ring} = 2.5. The sidelobes in this case do not impact the operation of a cascaded device since they do not appear

outside the maximum thermal tuning bandwidth. However, in a hypothetical design where they might be problematic, we note that the sidelobe suppression ratio (SLSR) can furtherly be optimized to become less than -25 dB by implementing an apodization design similar to that shown in Reference [64].

3.3 Device layout, fabrication and characterization

3.3.1 Silicon-on-insulator photonic chip

The miniaturized ring-grating spectrometer investigated here was designed and fabricated in a similar manner to that described in Reference [65], where a standard silicon on insulator (SOI) chip with a 250 nm device layer is employed. The designed structures are patterned into the device layer using a hydrogen silsesquioxane (HSQ) resist written by electron beam lithography (EBL) and etched using reactive ion etching (RIE). A 2-3 μm thick silicon dioxide (SiO_2) top cladding layer is then deposited by plasma enhanced chemical vapor deposition (PECVD). As illustrated in Figure 3.1, the miniaturized spectrometer consists of an add-drop ring resonator (radius = 5 μm) and static Bragg gratings. The width and the height of WG_1 is chosen to be 500 and 250 nm, respectively. The width and the height of WG_2 and the ring resonator-based add-drop filter waveguides are chosen to be 400 and 250 nm, respectively. By periodically modulating a portion of the WG_1 sidewalls by amplitude of 50 nm and the WG_2 sidewalls by amplitude of 40 nm, respectively the two DBR mirrors are created (see Figure 3.3). The two DBR mirrors are separated by a 250 nm gap and are formed out of 914 periods with a grating period, Λ=314 nm. The effective indices (n_1 and n_2) for both DBR waveguides (WG_1 and WG_2) were numerically found to be 2.535352 and 2.311079, respectively. These values are in good agreement with the theory Equation 3.1 in which the grating period was calculated and was found to be 313.6 nm. All input and output ports are tapered down to 170 nm in order to enhance the mode conversion during the edge

coupling of the input signal. Finally, since the thermo-optic effect in both structures are essentially identical there is no need to deposit large heaters (e.g., titanium-tungsten alloy) in order to tune the wavelength instead the entire chip is heated.

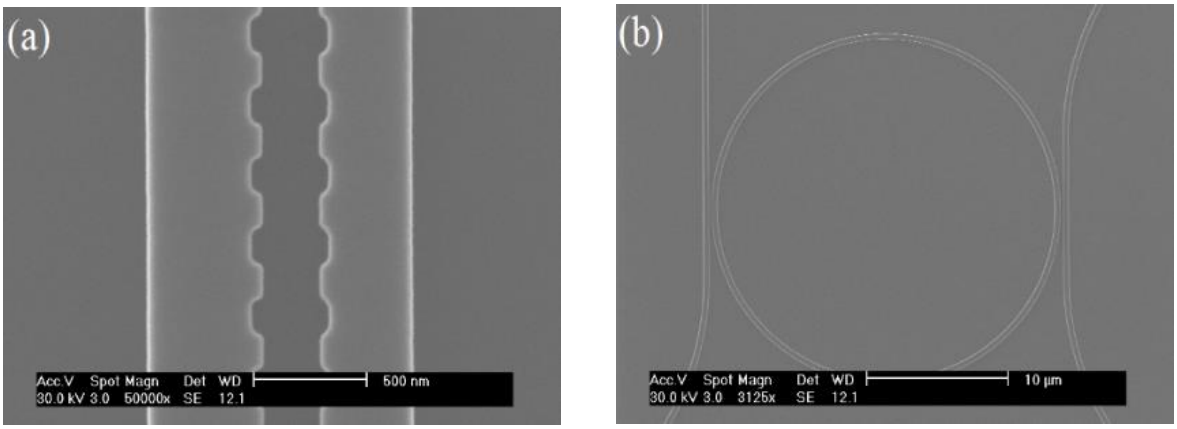

Figure 3.3: The uncladded scanning electron microscope (SEM) images of: (a) Distributed Bragg reflector filter (image scale 500 nm) (b) Add-drop ring resonator (image scale 10 µm).

3.3.2 Experimental setup

The characterization of the miniaturized spectrometer was performed using an upgraded version of the setup to that described in [65] (see Figure 3.4). A multifunction I/O device (USB-6212 by National Instruments) was integrated into the setup thus enabling the capability towards faster automation of the measurements by means of sweeping the laser wavelengths through a MATLAB program, which controls the trigger of both the source and the photodetector simultaneously. In addition, a temperature control device (TED200C by Thorlabs) is introduced to monitor and control the overall temperature on the chip through the thermoelectric cooler (TEC) and a thermistor located in close proximity to the sample.

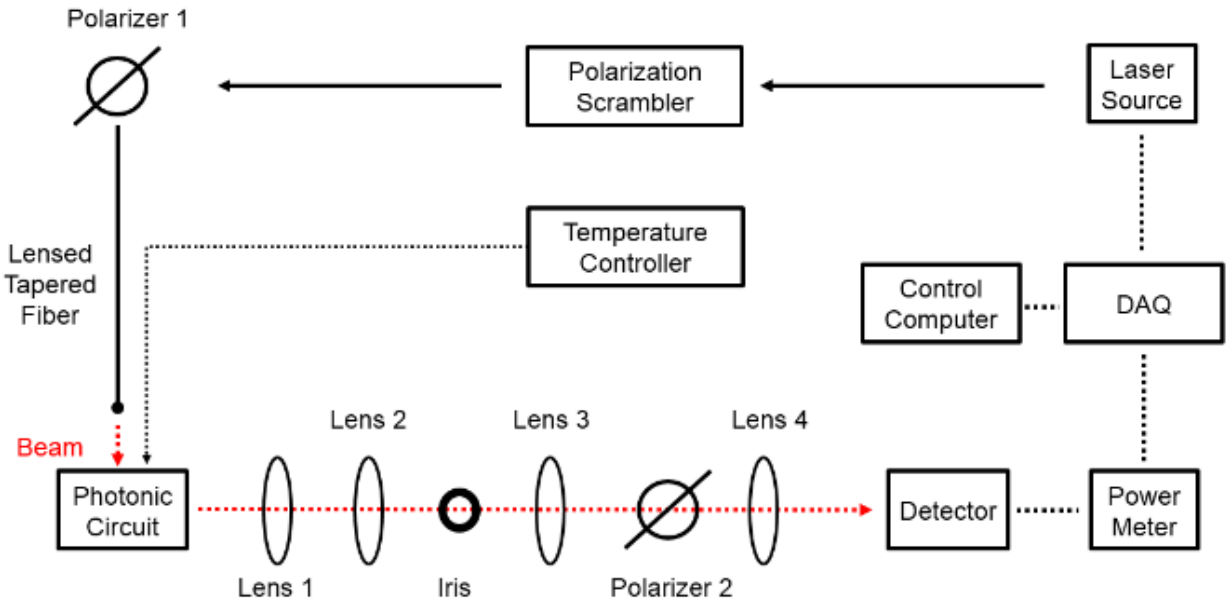

Figure 3.4: Setup used to characterize the sample.

3.4 Measurements and discussions

Due to fabrication variations (e.g., sidewall roughness, geometric deviation, etc.) shifts in the center wavelengths (λ_c, λ_1, and λ_2) of the distributed Bragg reflectors and the resonance wavelength (λ_{res}) of the add-drop ring resonator are anticipated. Figure 3.5 shows a noticeable shift of the center wavelengths of the stop band of the contra-directional coupling (DBR drop port) centered at 1516.2 nm (λ_c) while the resonance wavelength (λ_{res}) of the add-drop ring (ring drop port) is found at 1515.1 nm. The overall experimental spectral resolution and ER were found to be 0.121 nm and 19 dB, respectively (illustrated in Figure 3.6). Although the minimum insertion loss was found to be 27.7 dB in the current unpackaged device, it can be substantially decreased by implementing optical packaging with low loss couplers (i.e., to around 0.8-1.4 dB insertion loss [43]). Moreover, the time of acquisition of such a device can be made on the order of 1 ms as in Reference [66]. The design has a rich optimization space. The overall resolution can be substantially improved by employing a higher Q-factor ring resonator into the design, although

this must be balanced against a decrease in the SNR since the transmitted power will decrease. The ER aspect can be enhanced by lengthening the DBR elements or increasing the ring resonator Q-factor. Furthermore, depositing individual heaters on each element for future designs can rectify any local fabrication error for each of the individual elements hence enhancing the overall ER in the sense that the ring (i.e., λ_{res}) can be tuned towards the center of the DBR stop band thus enabling higher transmission (see Figure 3.5).

The discrepancy between the analytical model and the fabricated DBR (e.g., drop port and through port intensity) arises due to one of the following reasons: (i) the realignment of the fiber during each measurement; (ii) the misalignment of the fiber due to the thermal expansion [57]; (iii) different propagation length for each port (e.g., Through port ≈ 0.525 mm and Drop port ≈ 0.671 mm) indicating different propagation losses in which the waveguide loss and DBR loss are known to be 4.5 dB/cm [67] and 6 dB/cm [68], respectively; (iv) possibility of small random fabrication defects on the waveguides in addition to rough facets from dicing the sample which cause losses.

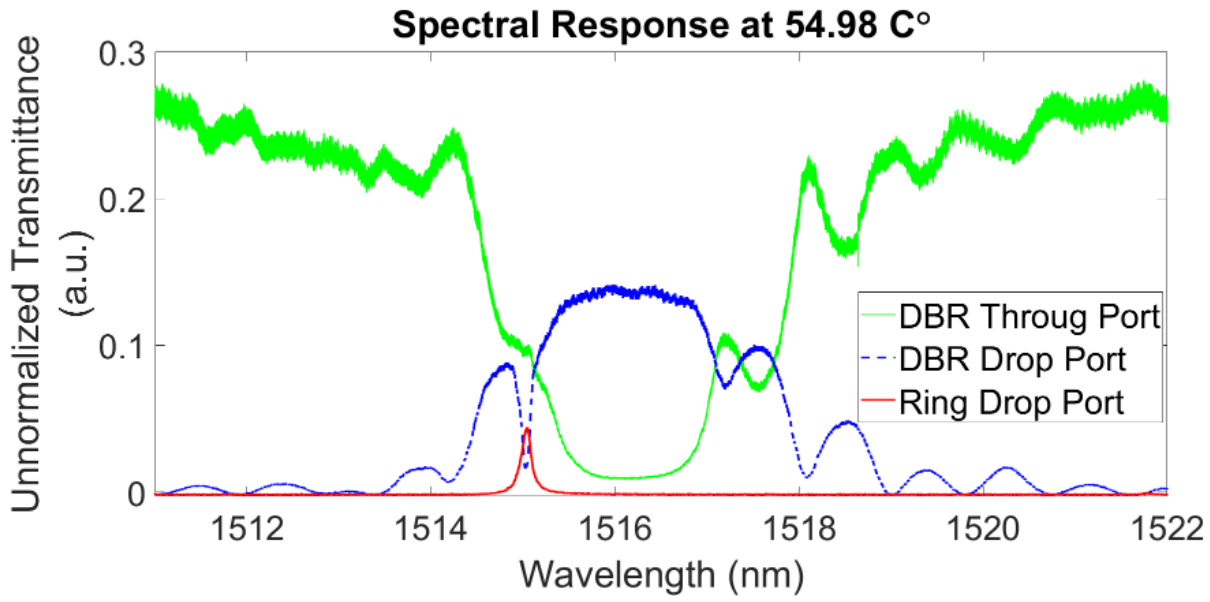

Figure 3.5: Experimental characterization of the fabricated ring grating spectrometer at 54.98 C°.

We use the thermo-optic effect in silicon to thermally tune the central wavelength of the stop bands (λ_c, λ_1, and λ_2) and the resonance wavelength (λ_{res}) of the ring resonator. Since the mode is highly confined, the thermo-optic effect in both structures are essentially identical, where $\frac{d\lambda_{DBR}}{dT} = 0.113\ \frac{nm}{K}\ and\ \frac{d\lambda_{ring}}{dT} = 0.115\ \frac{nm}{K}$, hence both elements can be simultaneously tuned. Moreover, CMOS compatible devices can tolerate high temperatures (i.e., 525 C^o) [69] hence tuning the free spectral range (FSR) of ring grating spectrometer (i.e., 30 nm) is quite achievable.

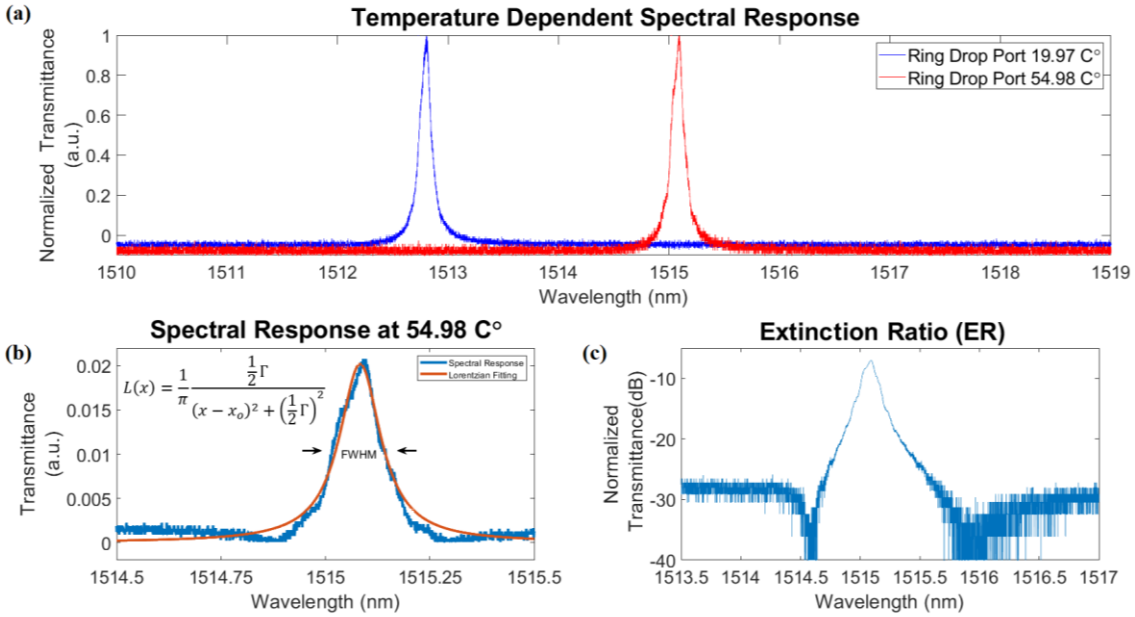

Figure 3.6: (a) Temperature dependence of the ring grating spectrometer response. (b) Spectrometer response at 54.98 C^o showing a FWHM of 0.121 nm. Here the spectral response of the ring was fitted with a Lorentzian function hence xo and Γ were used as the ring resonance wavelength (i.e., 1515.1 nm) and its full width half maximum (i.e., 0.121 nm), respectively. (c) Spectrometer response around 54.98 C^o showing an extinction ratio which is approximately 19 dB given optimal coupling.

The simulation results clarify that fabrication tolerance of ±20nm accounts for approximately -29.3 nm and 33.4 nm shifts in the stopband center, respectively. Similarly, the ring resonance shifts by -31.8 nm and +40.2 nm, respectively. To compensate for this an additional unit cell can be added above and below the nominal design to cover the desired spectrum, while the

ring resonance could be compensated by a local heating element. Smaller errors could be compensated by local thermal tuning alone.

3.5 Conclusion

In this work we demonstrated a miniaturized integrated ring-grating spectrometer that operates in the short-wavelength infrared (SWIR) spectrum which enables high spectral resolution (i.e., 0.121 nm) and high extinction ratio (i.e., 19 dB). Although the minimum insertion loss was found to be 27.7 dB in the current unpackaged device, it can be substantially decreased by implementing optical packaging with low loss couplers (i.e., to around 0.8-1.4 dB insertion loss). The device layer consists of an ordinary add-drop ring resonator (radius = 5 μm) in addition to a distributed waveguide Bragg reflector. The Bragg reflector employs a pair of waveguide sidewall gratings that form a broadband filter (i.e., 3.9 nm) which redirects a specific spectrum into an add-drop ring resonator, which behaves as a narrowband filter (i.e., 0.121 nm). The thermo-optic coefficients in both elements are essentially close to each other therefore both elements can be simultaneously tuned to analyze the spectra. The device is far more robust to local temperature variations than CROW devices, which are the nearest alternative. Furthermore, several unit cells with different central wavelengths could be stacked in a cascade in order to cover a broader spectrum bandwidth. The spectral resolution and ER of the device can be further improved by employing a higher Q-factor ring resonator in addition to lengthening the DBR element.

3.6 Acknowledgments

This chapter is in full, a reprint from the manuscript “Miniaturized integrated spectrometer using a silicon ring-grating design”, published in Optics Express, 2021, Naif Alshamrani, Andrew Grieco, Brandon Hong, and Yeshaiahu Fainman. The dissertation author was the first author in this manuscript and Yeshaiahu Fainman was the principal investigator. The authors would like to

thank Greg Vanwiggeren and Ryan Scott at Keysight for their fruitful discussions, and the Nano3 Staff at UCSD for their assistance during sample fabrication. Naif Alshamrani would like to thank King Abdulaziz City for Science and Technology (KACST) for their support during his study.

Chapter 4

Side-lobe reduction by cascading Bragg grating filters on a Si-photonic chip

4.1 Introduction

As silicon photonic devices continue their drive into the mainstream applications, the need for high contrast, compact Bragg-grating devices is ever-present. These devices offer great potential for large scale photonic integration due to their small foot-print and low fabrication costs in addition to flat-top response, low insertion loss and wavelength tunability. Over the years there have been tremendous efforts to design and optimize such optical filters [64,70–78]. One example is the all-pass filter decomposition approach by Madsen which has a large footprint and high fabrication complexity. In addition, many designs based on apodised Bragg gratings show excellent main-lobe to side-lobe contrast [64,70,79], but such devices achieve the high contrast at the expense of broadening the main lobe and increasing the device length. As shown by the prior work done in [70] and [64],the apodised designs are not only long (approaching 1 mm in length) but also compromise the bandwidth and spectrum profile.

This behavior is not surprising or novel. It was discussed extensively in Kogelnik's original work [80], where it was shown that for a same device length the side-lobe reduction is achieved at the expense of higher peak coupling coefficient of the grating and wider main lobe. It should be noted that the peak coupling in a grating can't be increased arbitrarily, since the theoretical model

relies on Perturbation theory to apply Coupled-mode equations. In [80] it is also shown that such devices are very sensitive to fabrication tolerances. In [80] when comparing Blackman and Kaiser apodization window functions, it is demonstrated how the two differ by less than 1% but their side lobes differ by 16 dB. In addition, to achieve lower side lobes the apodization needs to be extremely smooth which results in bigger device footprint, and which can be difficult to fabricate in commercial foundries. Additional relevant numerical calculations and simulations can be found in [81,82].

In this manuscript, we propose and experimentally demonstrate a novel method for reduction of side lobes via cascaded contra-directional couplers (CDC_S) utilizing Bragg gratings. As opposed to previous demonstrations, where such reduction is achieved via apodization of the Bragg grating, we design non-similar gratings in each of the contra-directional couplers. Each coupler is designed so that the null of the main lobe of the first grating coupler, overlaps with the peak of the side lobe of the second grating coupler. In our experiments, the gratings were tuned thermo-optically to match their central frequencies.

4.2 Theory and design

The effect of the periodic perturbation on a waveguide can be described by coupled-mode theory, which is noted in [83]. According to the coupled-mode theory the main effect of a periodic perturbation is to transfer energy from one mode to another. Such a transfer occurs when a difference between the mode wavenumbers is equal to that of the grating wavenumber, which is also known as the phase matching condition. Moreover, the strength of the coupling is determined by a quantity known as the coupling coefficient, which depends on the overlap between the interacting modes and the perturbation. For example, the periodic perturbation in direction of propagation x, the perturbation in permittivity can be decomposed into a Fourier series as follows

[82–84]:

$$\Delta\varepsilon\left(x,y,z\right)=\sum_{l}\Delta\varepsilon_{l}\left(y,z\right)\exp\left(-il\frac{2\pi x}{\Lambda}\right) \tag{4.1}$$

where Λ is the period of the perturbation, ε refers to the permittivity, l indicates the order of the Fourier series term in consideration, x, y and z are the cartesian coordinates. This can then be used in Equation 4.6 to determine the coupling strength between the modes of interest. In this work, only the first order perturbation term was taken into consideration and the periodicity of perturbation for each set of contra-directional couplers was set using Equation 4.7. The propagation constant (β_i) and the electric field profiles required for each mode in consideration can be calculated using any electromagnetic mode solver (i.e., LUMERICAL MODE). Once those above quantities are obtained, they can be substituted in Equation 4.6 and Equation 4.7 to obtain the coupling coefficient k_{lnm} and the periodicity of the perturbation Λ. Since wider waveguides have more confined modes, the overlap between modes is reduced. Finally, the differential equations govern such interactions are shown below [70,83,84]:

$$\frac{dA_1}{dx}=-jk_{11}A_2e^{j2\Delta\beta_1x}-jk_{12}B_2e^{j(\Delta\beta_1+\Delta\beta_2)x} \tag{4.2}$$

$$\frac{dB_1}{dx}=-jk_{12}A_2e^{j(\Delta\beta_1+\Delta\beta_2)x}-jk_{22}B_2e^{j2\Delta\beta_2x} \tag{4.3}$$

$$\frac{dA_2}{dx}=jk_{11}^{*}A_1e^{-j2\Delta\beta_1x}+jk_{12}^{*}B_1e^{-j(\Delta\beta_1+\Delta\beta_2)x} \tag{4.4}$$

$$\frac{dB_2}{dx}=jk_{12}^{*}A_1e^{-j(\Delta\beta_1+\Delta\beta_2)x}+jk_{22}^{*}B_1e^{-j2\Delta\beta_2x} \tag{4.5}$$

Where k_{11}, k_{22}, k_{12} are the coupling coefficients, * symbolizes a complex conjugate, A_1 & B_1 are forward propagating modes in each waveguide pair, while A_2 & B_2 are backward propagating modes. For CDC_1, A_m represent the modes in WG_1 while B_m represent modes in WG_2. Similarly,

for CDC_2, A_m represent the modes in WG_2 while B_m represent modes in WG_3. The methodology for solving above sets of coupled mode equations can be found in [70,83,84]. The above equations can be solved numerically, and the coupling coefficients can be varied to obtain the desired spectrum for each CDC. As mentioned before, the coupling coefficient can be tuned via multiple parameters like the gap between waveguides, the width of waveguide pairs, amount of perturbation. Then each individual CDC can be designed and simulated via FDTD or similar method to verify the functionality of the device and make any final adjustments before fabrication. In this case, only the waveguide width (WG_1 & WG_3) was altered and all other parameters except periodicity were kept identical for each CDC to minimize the effects of any fabrication variations/errors.

In general, two-phase mismatched modes don't undergo significant coupling. To transfer power between such modes, a Bragg grating based coupler relies on periodic perturbations. The perturbations determine the strength of coupling between the modes while the periodicity is chosen to compensate for the phase mismatch between the modes under consideration. The response of such devices usually consists of a strong main lobe and side peaks at frequencies that are unwanted in the design. Coupling strength is a primary contributor to the strength and the width of the main lobe. But, at the same time the strong coupling also contributes to the strength of the unwanted side lobes. To overcome this, devices with weaker coupling strength can be engineered [80,82]. Another solution is to apodize the coupling coefficient over the device length [64,70,79,80]. In such cases, the device length is increased significantly while also making the devices more susceptible to fabrication errors.

The device in consideration consists of three dissimilar waveguides on 220nm Silicon on Insulator (SOI) platform. They are enumerated as Waveguides 1, 2 and 3 and will be referred to

as WG_1, WG_2, and WG_3 from now on (see lay out shown in Figure 4.1). The dissimilar waveguide widths ensure phase mismatch between TE_0 modes of the closely spaced waveguides and hence there is little to no co-directional coupling as the light propagates in any of the waveguides. The Bragg structures are obtained by creating perturbations in WG_1 and WG_3 similar to these in [63]. The coupling between relevant modes can be calculated by [82]:

$$k_{\ln m} = \frac{\omega \iint \Delta\varepsilon_l (y,z)\left(E_m^* . E_n^*\right)\ dydz}{2\iint \varepsilon \left(E_m^* . H_n^*\right)\ dydz} \tag{4.6}$$

Here k_{lnm} describes the strength of coupling between the n^{th} mode and m^{th} mode due to the l^{th} order perturbation term, E_m refers to the electric field associted with the m^{th} mode, E_n refers to the electric field associted with the n^{th} mode, H_n refers to the magnetic field associted with the mode E_n, * symbolizes a complex conjugate, ω refers to the angular frequency of the optical field, ε refers to the permittivity, l indicates the order of the Fourier series term, x is the direction of propagation while y and z are coordinates in the transverse plane. It should be noted that in such devices, every mode strictly speaking interacts with every other mode. But over long interatction lengths phase mismatches lead to negligible average coupling between the modes. This leads to the need for periodicity in perturbation.

The effective indices were calculated for unperturbed waveguides using commercial simulation software LUMERICAL MODE. Then the periodicity of perturbations for each waveguide pair were calculated to compensate for the difference in propagation constants using [82,83]:

$$\beta_n - \beta_m - l\frac{2\pi x}{\Lambda} = 0 \tag{4.7}$$

where β_m refers to the propagation constant of the m^{th} mode along the propagation direction, x; β_n refers to the propagation constant of the n^{th} mode along x, l indicates the order of the Fourier series

term, and Λ is the period of the perturbation.

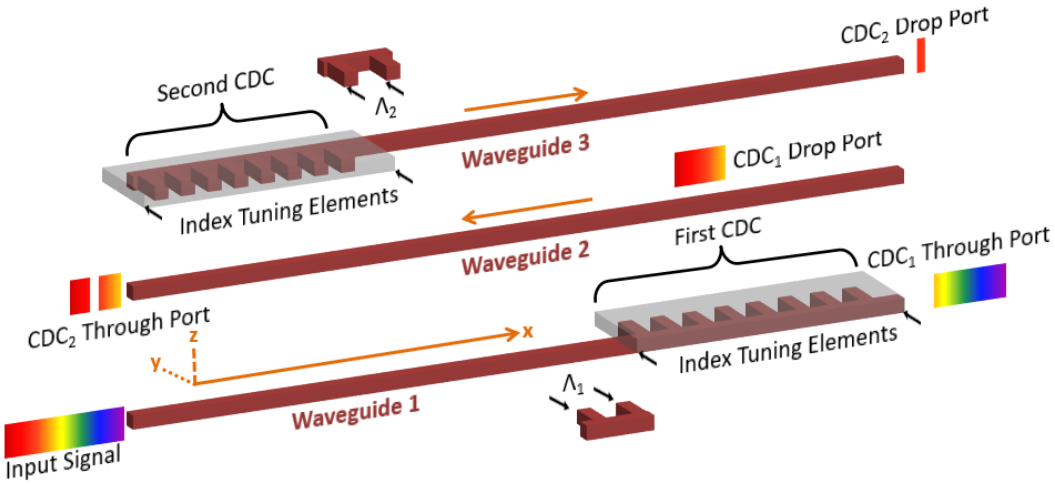

Figure 4.1: Conceptual schematic diagram of a cascaded contra-directional couplers (CDCs) device created through coupled Bragg gratings. In this design CDC_1 redirects a segment of the input signal from waveguide 1 (WG_1) into waveguide 2 (WG_2) while the remaining spectra passes through (CDC1 through port). Moreover, CDC_2 redirects the incoming signal from waveguide 2 into waveguide 3 (WG_3) such that the null of the main lobe of the first grating coupler, overlaps with the peak of the side lobe of the second grating coupler.

It should be noted that a stronger coupling coefficient between two modes leads to wider main lobes and higher side lobes. According to Equation 4.6 if the modes in consideration are more tightly confined to the waveguides, the coupling coefficient will be weaker since there will be less overlap with the perturbation. This device was designed for the worst-case scenario, where the first CDC has a wider main lobe which leaves the possibility of light being coupled into the side lobes for the second CDC. To this end, WG_1 was chosen to be narrower than WG_3. The intermediate waveguide WG_2 was chosen to be the narrowest of the three. This maximizes the possible coupling coefficients for each CDC while maintaining same gap between each waveguide pair. This also allows for shorter device length for each CDC. The mode in WG_3 being more tightly confined that the mode in WG_1 leads to the overlap and hence the coupling coefficient being stronger for the WG_1-WG_2 pair, compared to that of WG_3-WG_2 pair. This leads to a wider main lobe for the grating in the WG_1-WG_2 pair. More detailed analysis and derivation about the coupled mode theory treatment can be found in [79,82].

The simulation data in Figure 4.2 was obtained via 2.5D varFDTD simulations in LUMERICAL MODE. Each CDC had 600 periods which approximated to a device length of 0.19 mm per CDC. This was done to optimize the main lobe to side lobe contrast for each individual CDC. Beyond this point, the main lobe remained static, while the side lobes rose.

In this design the light couples from WG_1 to WG_2 via the first CDC (CDC_1). The main lobe for this CDC is wide. The light then encounters the second CDC (CDC_2) and gets coupled to WG_3. Here, the main lobe is narrower and the peak of the side lobe for CDC_2 overlaps with the minima of the main lobe for CDC_1. This leads to the reduction of the side lobe for CDC_2. It should be noted that it is essential to match the central wavelength for both CDCs. This ensures that the main lobes reinforce each other, and the strength of the main lobe remains unaffected for the light frequencies propagating in the cascade.

To ensure that the reduction of side lobes is being achieved by the overlap of minima of CDC_1 with the side lobe of CDC_2. Simulations were conducted where both WG_1 and WG_3 were the same. Consequently, both CDC_1 and CDC_2 have exactly same overlap. From Figure 4.2(a) there is still some extra reduction with the side lobe after CDC_2 being 4.46 dB lower than the side lobe after CDC_1. But, for the device comprising of dissimilar CDCs, the side lobe is suppressed by 6.71 dB after CDC2 compared to the side lobe after CDC_1. As a result, the device with dissimilar CDCs has a side lobe reduction of 11.17 dB compared to 8.43 dB for similar CDCs. Hence, the effect of overlap between minima of main lobe and the maxima of the side lobe was verified.

Most importantly, the minimizing process of variation between the two CDCs was considered as a major impetus for the compact device design. Moreover, changes in the central wavelengths of the main lobe were observed while varying the minimum mesh size. This change

becomes minimum after a certain number of mesh points. However, as we refine the mesh numerical error at each calculation point this also could lead to errors in simulations. From there, heaters were included even after performing the simulations at a very high level of mesh refinement.

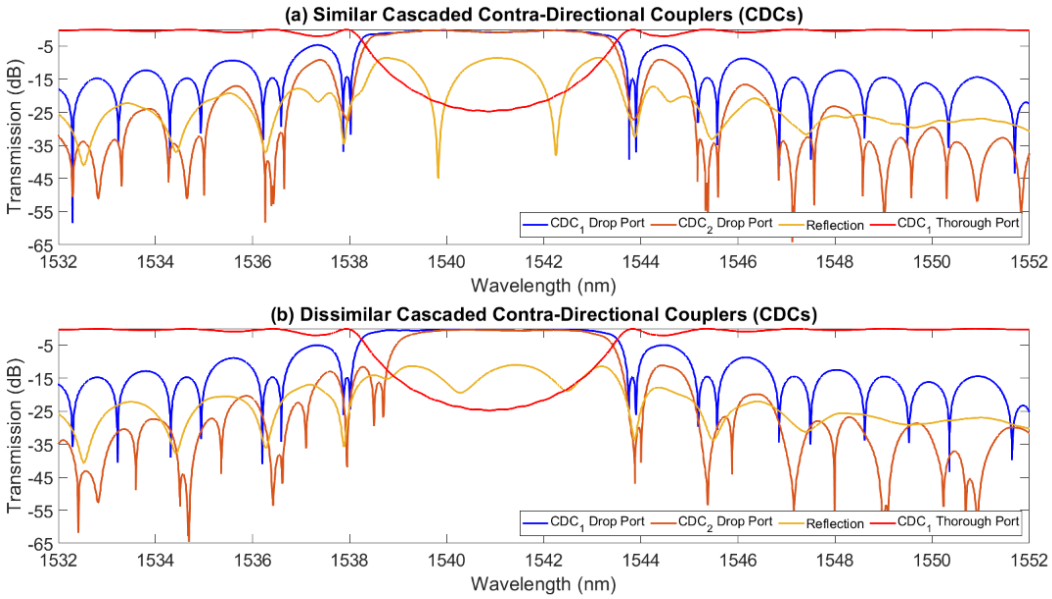

Figure 4.2: LUMERICAL MODE - 2.5D varFDTD simulations of: (a) Similar cascaded contra-directional couplers (CDCs) in which the side mode reduction ratio of redirect segment of the incoming signal (through CDC_1) is approximately 3.97 dB and is lowered down to approximately 8.43 dB (through CDC_2). (b) Dissimilar cascaded contra-directional couplers (CDCs) in which the side mode reduction ratio of the redirect segment of the incoming signal (through CDC_1) is approximately 4.46 dB and is lowered down to approximately 11.17 dB (through CDC_2).

4.3 Fabrication and characterization

The -SOI device investigated in this manuscript was fabricated as part of a multi-project-wafer (MPW) run at the Applied Nano Tools foundry, Edmonton, Alberta, Canada [30]. In which a standard silicon on insulator (SOI) wafer with a 220-nm device layer is coated with a soft mask. The structures are then transferred into the device layer (fully etched) via electron beam lithography (EBL) and reactive ion etching (RIE). Plasma enhanced chemical vapor deposition (PECVD) is then employed to clad the sample with a thick layer (e.g., 2.2 µm) of silicon dioxide

(SiO2). Heaters are then formed by depositing Titanium-tungsten alloy (TiW) over the static Bragg gratings in order to tune the stop bands hence overcoming the overall fabrication variations. Titanium-tungsten aluminum bi-layers are then employed to route the heaters with contact pads. The device is then cladded with a thin layer (e.g., 300 nm) of silicon dioxide (SiO2), which protects the heaters from oxidation. Small windows are opened on top of each pad via RIE [11]. The overall chip was designed to meet the design rules of Applied Nanotools where a complete listing of design rules and layout tools are reported in [30,37]. Moreover, detailed information regarding the fabrication process can be found in [30].

As illustrated in Figure 4.1 and Figure 4.3, The device consists of two static Bragg gratings (WG_1 and WG_3) and a mid-waveguide (WG_2) which is placed in between them. The width of the lower waveguide (WG_1) is chosen to be 500 nm where a portion of its sidewalls is periodically modulated by ± 25 nm and its grating period, Λ=320 nm with a 50% duty cycle (DC). The width of the upper waveguide (WG_3) is chosen to be 570 nm in which a portion of its sidewalls is periodically modulated by ± 25 nm and its grating period, Λ=315 nm with a 49.2% duty cycle (DC). Both contra-directional couplers are formed out of 600 periods and are separated by a 200 nm gap from the 400 nm wide mid-waveguide (WG_2). The simulation results presented in Figure 4.2(b) correspond to the final fabricated design.

The characterization of the side lobe reduction device was performed using a fiber-to-free space setup described in [12,65]. Moreover, the input/output waveguides on the chip were inversely tapered down to approximately 180 nm in an attempt to enhance the overall mode conversion of the beam while coupling light from this setup. In addition, the CDCs were separated by approximately 40-45 um thus ensuring thermal isolation between them when tuning one of the individual heaters. This spacing was found to be sufficient according to LUMERICAL DEVICE

Multiphysics Simulation (HEAT solver). Optimized heaters and trenches can then be employed in future devices that require even higher temperatures (tuning) or more compact designs.

4.4 Device performance

Without any adjustment to the heaters, the central wavelength for the CDCs main lobes were observed to be misaligned due to fabrication variation (as seen in Figure 4.4(a)). In this case, CDC_2 Through port indicates the spectrum for CDC_1 Drop port. This was expected and was the primary impetus for the heaters being included in the design. Once 3.9 DC voltage (18.6 mA) was applied to the heater over CDC_1 the central wavelengths for both CDCs were aligned (see Figure 4.4(b)). As it can be observed from Figure 4.4(a), the side lobe for CDC_1 is approximately 5.57 dB below the main lobe. Once the CDCs are appropriately aligned, the side lobe for CDC_2 approximately overlaps with the null of the main lobe for CDC_1. As a result, the side lobe drops to 12.93 dB below the main lobe. This is a 7.36 dB improvement over the original performance of CDC_1.

4.5 Discussion and conclusion

According to the simulations, the device shown here performs 2.74 dB better than a simple cascaded design. It should also be noted that for simple cascaded design, WG_1 and WG_3 will need to be placed a considerable distance apart to prevent any co-directional coupling. Another disadvantage for such design would be the potential for Fabry-Pérot resonances. Moreover, in contrast to existing apodised designs with device lengths of around 1mm, the novel dissimilar CDC cascade design has a much smaller footprint of 0.4mm total length and a more controllable and predictable transmission spectrum. The compact nature of this design will allow for prevention of fabrication errors introduced in larger devices. In addition, the cascaded CDC design also doesn't broaden the main lobe of the device.

The design principal can be boiled down to reinforcement of main lobes by matching their centers while diminishing the side-lobes by overlapping the maxima of one coupler with the minima of the other. This basic principle can potentially be used to create devices with even better spectral characteristics if they require multiple CDCs or DBRs. One such widely popular use case would be the design of a DBR based laser cavity. When designing such a cavity, shorter DBR sections can be designed. Each DBR in this case will have worse main lobe to side lobe contrast compared to longer devices. However, if each of the DBRs is designed following the above design principle. The design could provide for a compact device with equal or better performance compared to a device with identical DBRs that have weaker coupling but are substantially longer. The design is highly adaptable and can also be used in case apodized DBR are required to meet performance specifications. Even when using apodized DBR, the individual DBR can be more compact leading to a smaller device footprint. It should also be noted that this device is expected to have slightly weaker reduction in one direction. In case of DBR lasers, such concerns will be minimized, since only the narrower main lobe that is being reinforced will survive multiple roundtrips in the cavity. The compact nature will allow for more reliable fabrication of these devices. This in turn will lead to better yields and lowering the cost per device and making the devices more market ready.

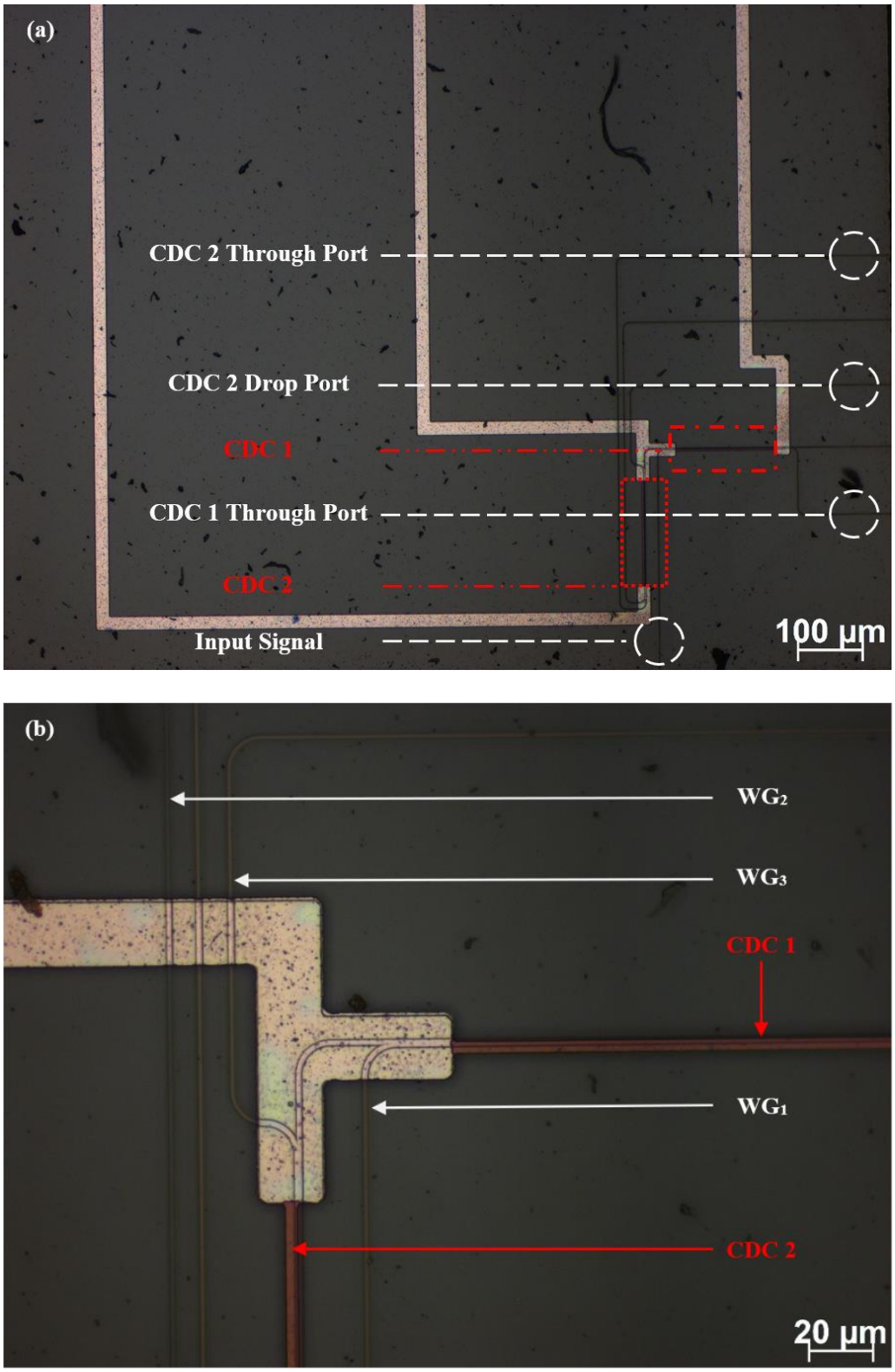

Figure 4.3: Microscopic images of the chip showing: (a) The different input and output ports in addition to the two contra-directional couplers (image scale 100 µm). (b) The various waveguides (WG_1, WG_2, and WG_3) which create the two contra-directional couplers (image scale 20 µm).

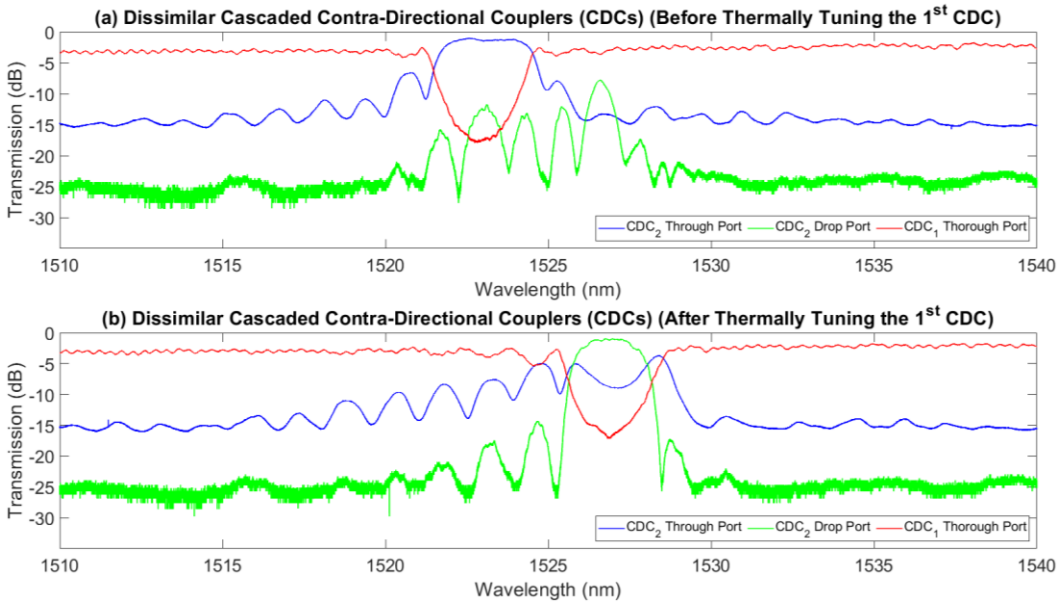

Figure 4.4: Experimental characterization of the fabricated cascaded contra-directional couplers (CDCs): (a) Before thermally tuning the first CDC hence the central wavelength of the main lobe was misaligned in comparison to the second CDC (due to fabrication variation), therefore the side lobe of the second CDC does not overlap with the null of the main lobe (first CDC). In this case, CDC_2 Through port indicates the spectrum for CDC_1 Drop port. (b) After thermally tuning the first CDC hence the central wavelength of the main lobe aligns with that of the second CDC, therefore the side lobe of the second CDC overlaps with the null of the main lobe of CDC_1.

4.6 Acknowledgments

This chapter is in full, a reprint from a manuscript “Side-lobe reduction by cascading Bragg grating filters on a Si-photonic chip”, published in Optics Express, 2022, Sushant Kumar, Naif Alshamrani, Andrew Grieco, and Yeshaiahu Fainman. The dissertation author was a co-first author in this manuscript and Yeshaiahu Fainman was the principal investigator. Naif Alshamrani would like to thank King Abdulaziz City for Science and Technology (KACST) for their support during his study.

Chapter 5

Fabrication-tolerant Fourier transform spectrometer on silicon with broad bandwidth and high resolution

5.1 Introduction

Fourier transform spectrometers (FTSs) recovering an unknown spectrum are powerful tools in various fields including chemical sensing, bio-medical applications, and autonomous vehicles, etc. [59,85–87]. Compared to other direct-detection-based spectrometers, such as monochromators or grating-based spectrum analyzers, one of the key advantages of FTSs is Fellgett's advantage, namely, higher signal-to-noise ratio and dynamic range [88]. The FTS employs an interferogram (i.e., autocorrelation function) generated from the input signal with unknown spectra using an interferometer, where the input signal is divided into two paths with variable optical path difference (OPD). At the output of the interferometer, the optical signals from these two optical paths are recombined on a photodetector, which is used to generate a photocurrent as a function of OPD, thereby generating the desired interferogram. The Fourier transform of the detected interferogram (i.e., autocorrelation function) produces the power spectral density of the input signal. The larger the maximum OPD, the higher the spectral resolution. A classical FTS typically uses a moving element (such as a mirror) to introduce quasi-continuous tunable OPD

between two paths and generates a temporal interferogram (i.e., autocorrelation function). Thus, FTSs are usually realized as bulky free-space interferometric systems and suffer from slow scanning speeds, resulting in long measurement times.

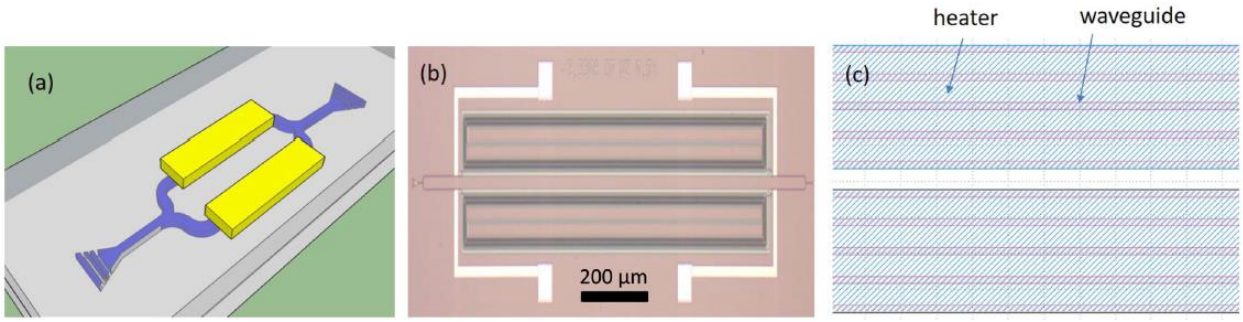

Figure 5.1: (a) Schematic and (b) microscopic image of the fabricated device. (c) Zoom view of the waveguides and heater. The waveguide is designed to have a serpentine shape to reduce the footprint, and the heater has a width of 17 µm that covers five waveguides in order to maintain low resistance.

Use of silicon photonics as a platform for FTS realization has attracted widespread attention as a candidate to meet the rapidly growing demand for low-cost, portable devices [89]. In contrast to free-space FTSs, most FTSs demonstrated on silicon platforms are spatial heterodyne spectrometers (SHSs) that employ a large array of unbalanced Mach–Zehnder interferometers (MZIs) with varying length differences, each of which introduces a fixed amount of OPD to the spectrum [59,90–92]. In order to achieve high resolution (i.e., large OPD), the incident spectral signal is typically required to be split into over 50 MZIs with predetermined delays, resulting in a considerably large footprint, large insertion loss, low dynamic range, and low signal-to-noise ratio. SHSs also usually support a narrow bandwidth (i.e., a few 100 pm) despite its very high resolution (a few 10s of pm) [90]. An alternative approach, called stationary FTS, generates a spatial interferogram utilizing a standing wave pattern between two co-propagating waves [93]. Compared to the SHS approach, it is demonstrated to trade-off a significantly reduced footprint and broad operating bandwidth (100 nm) for very low resolution (6 nm). Moreover, a dense array of photodetectors is required to be fabricated on top of the structure plane to capture the spatial

interferogram, which significantly limits scalability, increases integration complexity, and perturbs the spatial interferogram [93].

Recently, an analogue to classical FTS on silicon that generates a temporal interferogram by quasi-continuously tuning the OPD between two arms of a single MZI was demonstrated [57]. As shown in Figure 5.1, tuning of the OPD is achieved by applying electrical power to an integrated heater above the waveguide to create a phase shift using the thermo-optic effect in one of the two MZI arms. To achieve a moderate spectral resolution (3 nm) with a feasible temperature change, the waveguide length was designed to be 3 cm. To keep a compact footprint, the waveguide was designed to have a serpentine geometry. This device was shown to operate with large band width signals (>60 nm), limited only by the bandwidth of the input coupler of the waveguide and the transmission window of the optical materials. In comparison with SHS and stationary FTS, this temporal heterodyne spectrometer (THS) [57] has the advantages of operation with broad bandwidth signals, compact footprint, high dynamic range, and compatibility with chip-scale integration, making it a promising candidate for portable, broadband, low-cost FTSs. A major disadvantage of TSH lies in the demonstrated spectral resolution (so far,3 nm or 0.38 THz), which is insufficient for many applications, and the research to tackle this problem remains scarce. In theory, the resolution of a single THS could be increased by supplying higher power to the heater or implementing a longer waveguide, which are both non-trivial approaches for centimeter(cm)-scale waveguides. High power injection to the heaters will aggravate thermal structural expansion, raise the risk of shortening the device lifetime, and jeopardize heater integrity. Other disadvantages include large resistance (over 10 kΩ) for long heaters, making them impractical to operate at high electrical power, whereas longer waveguides will affect and limit the sensing dynamic range and the signal-to-noise ratio. Alternatively, the resolution could be improved using a circuit level

technique by deploying a silicon microring resonator in front of the THS that selectively sends a narrow band of the incident signal to the THS for processing [94]. The resolution is improved to 0.47 nm, but this technique is very similar to those direct-detection approaches that sacrifice the SNR of the THS.

In this paper, by engineering the waveguides to reduce propagation loss and optimizing the heater design to accommodate higher power actuation, we demonstrate a higher spectral resolution THS [57]. The device utilizes broader multi-mode waveguides in the straight section of the serpentine wave guide to reduce the propagation loss while reducing the waveguide width at bending sections to 500 nm to avoid modal crosstalk and retain a compact footprint. With the reduction of propagation loss, the serpentine waveguide length is increased from 3 cm in THS from Reference [57] to 10 cm, and the heater design is improved so that the total resistance is reduced to around 5 kΩ, compared to 15 kΩ in Reference [57] with more coverage of the waveguides. This technique has been applied in other applications such as high-Q resonator and microwave filters [95,96], but we realize that there is a prolific body of work in spectrometers in which this technique is not used [59,90,92,94,97]. Our experiments demonstrate a spectral resolution of 0.11 THz or sub-nanometer (nm), more than 3 times higher than that in the previous demonstration [57] while maintaining a broad bandwidth of operation with a compact footprint. Moreover, we investigate and prove, through both simulations and experimental results, that fabrication variations imposed on standard single-mode waveguides degrade the performance of silicon THS or even deteriorate their functionality, while using wide waveguides in the MZI arms of the current design not only reduces optical loss but also significantly reduces the effect of fabrication errors.

5.2 Device design and simulation

As discussed in Section 5.1, to increase the spectral resolution of FTSs, the maximum achieved OPD should be increased using longer waveguides. Conversely, longer waveguides result in a higher signal insertion loss, which decreases the dynamic range of the device. To maintain a high dynamic range, the propagation loss needs to be reduced. The main source of losses in silicon waveguides is due to scattering on the waveguide-sidewall roughness, which is inevitable due to the limitations of current fabrication technology [98,99].

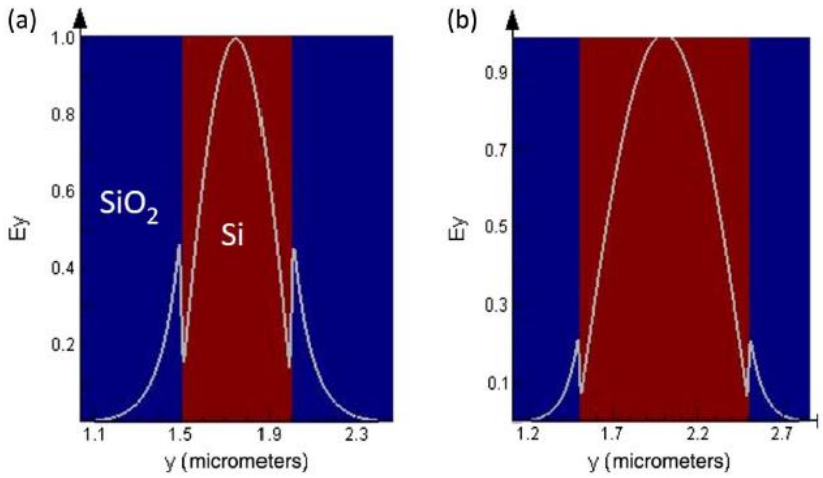

Figure 5.2: Simulated E_y intensity of the TE mode in (a) a 0.5 μm wide waveguide and (b) a 1 μm wide waveguide. The thickness is 220 nm.

A typical electric field distribution for TE-like propagating mode in a 500 nm wide and 220 nm high silicon waveguide is shown in Figure 5.2(a). It is evident that a strong electric field on the waveguide sidewalls will interact with its roughness and excite undesired unguided modes (radiative loss) or back-propagating modes (stochastic backscattering). Besides, a long-silicon-strip waveguide has been reported to exhibit extremely strong fluctuations in its transmission spectrum, which is also attributed to sidewall roughness [100]. One effective technique to reduce the roughness-induced issues is to reduce the electric field amplitude on the waveguide sidewalls

by using a wide waveguide [see Figure 5.2(b)]. We use this approach in our FTS serpentine arm design to reduce the losses and increase its length. Specifically, the straight sections of the serpentine arm are engineered to be 1 μm × 220 nm cross-section strip waveguides with low propagation loss, whereas the bending sections are implemented using strip waveguides with a 500 nm × 220 nm cross section to avoid excitation of unwanted higher-order modes and also keep a tight bend radius (i.e., 5 μm) with negligible bending loss [101]. The transition between the multi-mode and single-mode waveguides is achieved using an adiabatic linear taper with a length of 4 μm that exhibits negligible loss and reflection.

In this low-loss design, we also increased the serpentine waveguide length to 10 cm, such that at the same temperature change, we could expect more than 3 times increase in OPD compared to that used in Reference [57], which will result in about 3 times increase in resolution. Also, the corresponding serpentine heater benefits from the improved design to more efficiently cover the waveguides while keeping the total resistance down to a few kΩ, making it suitable for operation with our voltage source, which is limited to 210 V. The serpentine heater has a width of 17 μm and a total length of 2.3 cm covering the entire 10 cm long waveguide [shown in Figure 5.1(c)]. The simulated performance of the FTS with 3 cm long arms and 10 cm long arms is plotted in Figure 5.3(a) - 5.3(d). Given the same temperature change of 60 K, the current 10 cm device leads to a spectral resolution of 0.14 THz, which is more than 3 times higher than that obtained with the 3 cm device.

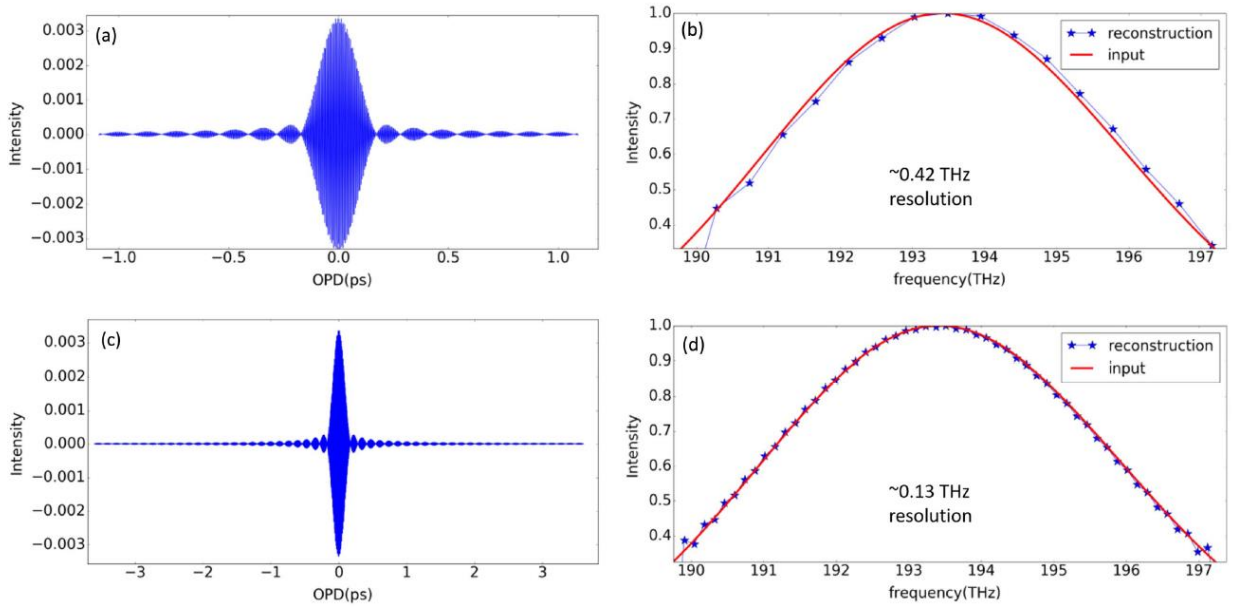

Figure 5.3: Simulated interferograms and recovered spectra from two different devices: (a), (b) a balanced MZI with waveguide length of 3 cm; (c), (d) a balanced MZI with waveguide length of 10 cm. For both devices, the maximum temperature change is 60 K. Their individual spectral resolutions are 0.42 THz and 0.13 THz, respectively.

Besides the enhancement of spectral resolution, another issue that has been neglected is fabrication variation on the waveguide width. In the work reported in Reference [57], the center of the interferogram is shifted to 0.172 ps due to the fabrication variation- induced differences in the two arms. The FTS works, as the variation is relatively small such that the temperature change caused by the heater (55 K) could make the device meet a zero-OPD (center of the interferogram) condition. However, the device was fabricated using electron beam lithography, which induces smaller variations in waveguide dimensions compared to optical lithography, which is the main choice for CMOS foundries. Moving towards a mature THS-on- silicon platform, the fabrication variation should be thoroughly studied and taken into consideration. According to wafer- scale characterization of manufacturing variability for silicon photonics components [102], the typical width variation in a strip waveguide can be as large as 20 nm. To study the impacts of such a large fabrication variation, a series of simulations were performed for two devices: an MZI with waveguide widths of 0.5 μm and 0.52 μm and an MZI with widths of 1 μm and 1.02 μm. For both

devices, the arm length is 10 cm and the maximum temperature change is 60 K. The results are plotted in Figure 5.4. Compared to the imperfection-free device, shown in Figure 5.3(c) and Figure 5.3(d), the interferogram of the device with 0.5 μm and 0.52 μm waveguide widths does not contain the zero-OPD information, and thus the spectrum reconstruction fails [Figure 5.4(a) and 5.4(b)]. This is due to a 20 nm variation in the 500 nm waveguide width, which translates to an effective index difference of 0.02. A 60 K temperature change only induces a index change of 0.01 and thus cannot compensate for this index difference. On the other hand, using wide waveguides with 1 μm width, with the same fabrication variation present, the effective index difference is as small as 0.003. Consequently, the interferogram shifts away from the origin but still contains the zero-OPD information, and thus the spectrum can be successfully reconstructed [Figure 5.4(c) and 5.4(d)].

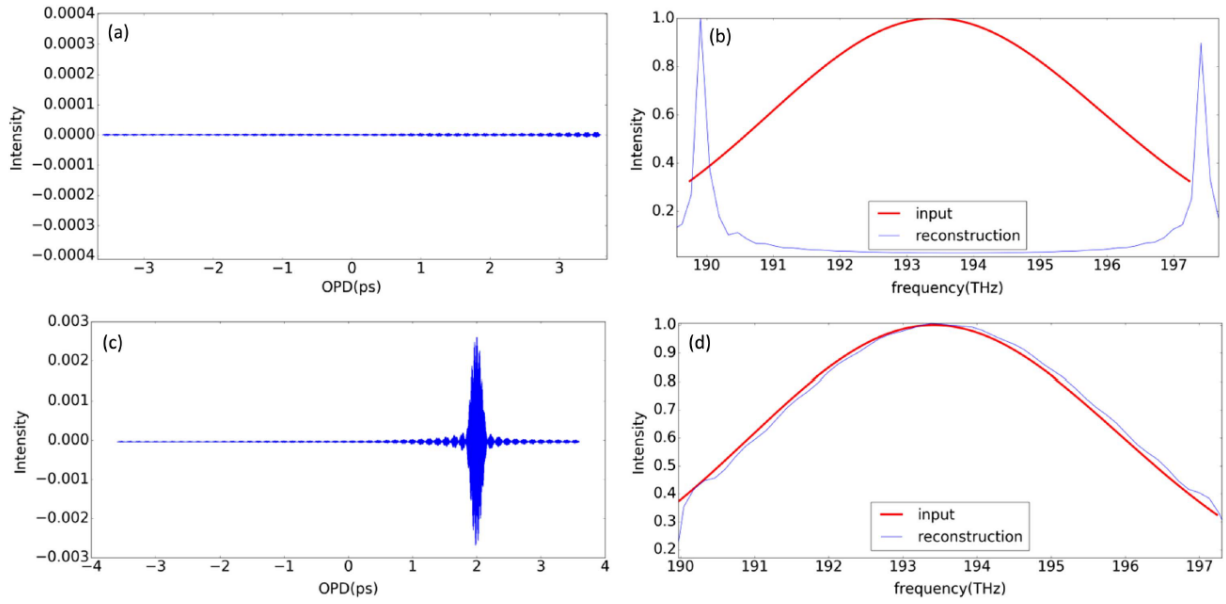

Figure 5.4: Simulated interferogram and recovered spectrum from two different devices: (a), (b) a balanced MZI with slightly different waveguide widths for the two arms (0.5 μm and 0.52 μm); (c), (d) a balanced MZI with slightly different waveguide widths for the two arms (1 μm and 1.02 μm). The 20 nm width difference corresponds with typical fabrication variation. For both devices, the arm length is 10 cm and maximum temperature change is 60 K.

5.3 Experimental results

The devices were fabricated through a multi project wafer (MPW) service at a commercial foundry (Applied Nanotools) with electron beam lithography, and thus the fabrication variation in the waveguide width becomes negligible compared to our intentional variation of 20 nm. Grating couplers are employed as the fiber/chip coupling components. Characterization of waveguide propagation loss with widths of 0.5 μm and 1 μm is given in Figure 5.5. All waveguides have the same serpentine type as used in our THS. Clearly, for our 10 cm long FTS, using 1 μm wide waveguides could increase the dynamic range about 8.5 dB. The measured heater resistance is about 5 kΩ.

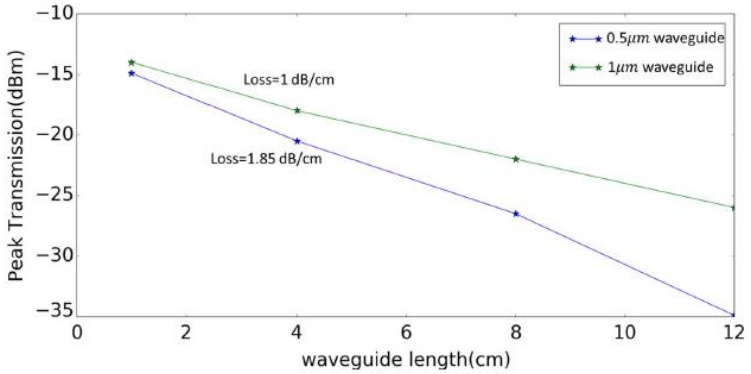

Figure 5.5: Cutback method to characterize two different types of strip waveguides with 0.5 μm width and 1 μm width.

Following the calibration procedures reported in Reference [57], we aim at reconstructing the spectrum of an ASE source (C+L band). The results of a perfectly balanced FTS (1 μm arm width and 10 cm arm length) are plotted in Figure 5.6. In Figure 5.6(a), the raw data of the measured interferogram as a function of power injection to the heaters is present. The positive/negative sign of the x axis refers to actuation of the top/bottom heater. The raw data exhibits a modulated envelope due to the thermally induced chip expansion that modifies the grating coupler performance and thus the overall coupling efficiency. The maximum power

injection is about 5.2 W, corresponding with a voltage supply at 160 V. Even though our equipment can deliver voltage up to 210 V, the strong thermally induced chip expansion decreased the power collected by the photodetector to noise floor levels as evident in Figure 5.6(a). The post-processed interferogram [Figure 5.6(b)] is almost centered at zero OPD, indicating negligible fabrication variation between the two arms. The reconstructed spectrum matches with the original spectrum well [Figure 5.6(c)] with a spectral resolution around 0.11 THz [Figure 5.6(c)], more than 3 times enhancement compared to the previous demonstration [57].

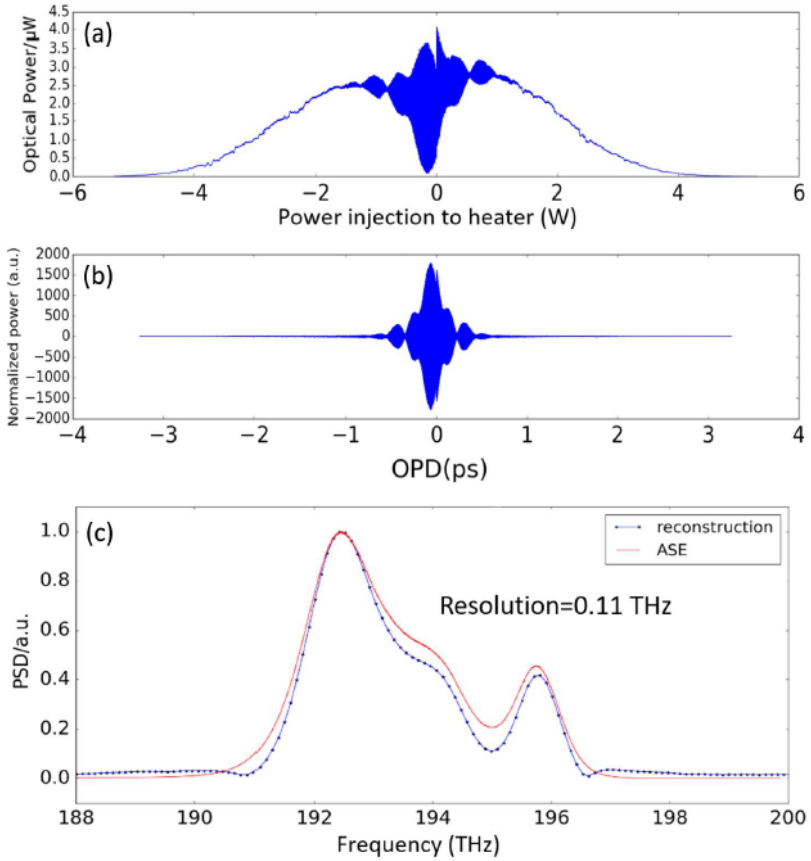

Figure 5.6: Experimental results of a balanced FTS with identical arm widths of 1 μm. (a) Raw data of the interferogram as a function of power injection to the heaters. The sign in the x axis refers to the actuation of different heaters. (b) Plot of the post-processed interferogram ready for Fourier transformation. (c) The reconstructed spectrum compared with the original input spectrum.

The resolution could be further improved by injecting more power into the device once the thermally induced expansion is resolved. The small discrepancy between the retrieved spectrum

and the input spectrum shown in Figure 5.6(c) is a result of multi-source instabilities during the measurement procedure. For instance, the input and output fibers can show certain drift during the 1.5 h long measurement period, which leads to slightly inaccurate optical power collected by the detector. Also, in the current setup, the electrical probes are attached to the electrical pads without firm bonding. Therefore, during the measurement period, especially at high power injection to the heater, the thermal expansion might cause the contact between the probes and the on-chip pads to become unstable, resulting in inaccurately monitored power injection to the heaters. All these minor issues could be effectively solved once the chip is packaged, such that the fibers and electrical probes would be firmly attached to the silicon chip during the measurement.

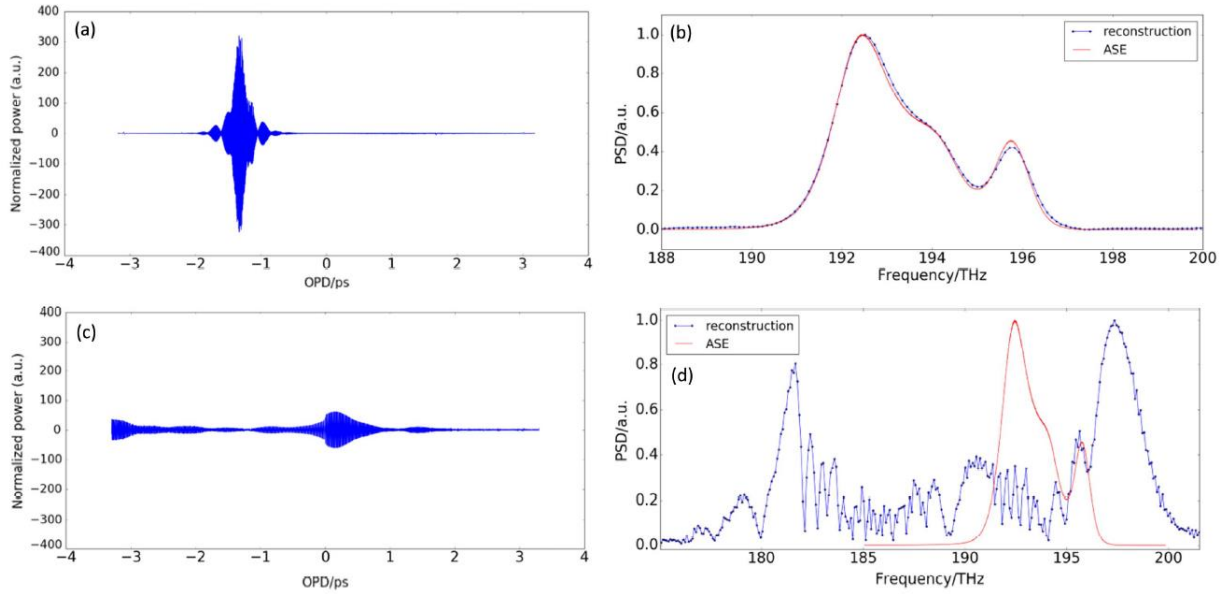

Figure 5.7: Experimental results of impacts of fabrication variation on a balanced FTS. (a), (b) Interferogram and spectrum reconstruction of a balanced FTS with arm widths of 1 μm and 1.02 μm. (c), (d) Interferogram and spectrum reconstruction of a balanced FTS with arm widths of 0.5 μm and 0.52 μm. The 20 nm difference in the two arms represents the fabrication variation in CMOS technology. Clearly, the device using a large waveguide width is tolerant to this amount of variation, while the 0.5 μm device fails to reconstruct the spectrum.

The experimental results of the fabrication-tolerant device are given in Figure 5.7. Figure 5.7(a) and 5.7(b) show the interferogram and spectrum reconstruction of a balanced FTS with arm widths of 1 μm and 1.02 μm, while the interferogram and spectrum reconstruction of a balanced FTS with arm widths of 0.5 μm and 0.52 μm are plotted in Figure 5.7(c) and 5.7(d). The 20 nm

difference in the two arms represents the fabrication variation in CMOS technology. For 1 μm waveguide, this amount of width variation leads to a much smaller effective index change (around 0.003 based on simulations), and the interferogram still contains the zero-OPD regime; thus, the spectrum could be successfully reconstructed. For the device with 0.5 μm width, 20 nm variation in the waveguide width could completely shift the zero OPD out of the measured interferogram, resulting in a failure in spectrum reconstruction.

5.4 Conclusion

In this paper, we report our follow-up work in silicon FTSs with a focus on resolution enhancement and fabrication tolerance. By using hybrid waveguides in the serpentine section with reduced propagation loss and improved heater design, the maximum achievable OPD between the two arms is increased, leading to increased resolution, which is confirmed by experimental data: 0.11 THz resolution is achieved compared to the previous demonstration of a resolution of 0.38 THz [57]. Also, for the first time to our knowledge, we draw the attention to the impacts of fabrication variation on this kind of device and demonstrate that using our technique could make the device tolerant enough for CMOS technology, paving the way for a commercial product.

5.5 Acknowledgments

This chapter is in full, a reprint from the manuscript “Fabrication-tolerant Fourier transform spectrometer on silicon with broad bandwidth and high resolution”, published in Photonics Research, 2020, Ang Li, Jordan Davis, Andrew Grieco, Naif Alshamrani, and Yeshaiahu Fainman. The dissertation author was a co-author in this manuscript and Yeshaiahu Fainman was the principal investigator.

Chapter 6

Multifunctional photonic biosensors with information fusion for blood glucose sensing

To this end, we propose a multifunctional photonic biosensor with information fusion. The device will leverage recent progress on integrated spectroscopy and fiber sensors to be inexpensive, accurate, portable, and extensible.

6.1 Proposed technical approach

6.1.1 Fabrication and material system

The material system is the most important consideration when designing integrated photonic sensors, as the spectral transmission window places hard limits on the available wavelengths [103,104]. Furthermore, the foundry availability of the fabrication processing techniques will have a major impact on the ultimate cost of the device. All things considered; silicon nitride is the single most attractive platform for this application. It provides a transmission window from the near-ultraviolet to the near-infrared, and it has a high optical power tolerance. Additionally, it has a mature fabrication process, and is available from many foundries. If hybrid material platforms are considered, silicon nitride can be integrated with silicon and germanium to cover much of the mid-infrared spectrum [103,104].

Consideration should also be given to the economy of the necessary optical sources and detectors. High power optical sources and high speed, sensitive detectors are readily available for

low cost in the ultraviolet, visible, and near infrared. Sources and detectors in the mid-infrared are more costly, and the detector speed becomes slower. This further reinforces the selection of silicon nitride as the platform of choice, as the transmissions window corresponds with the best value components.

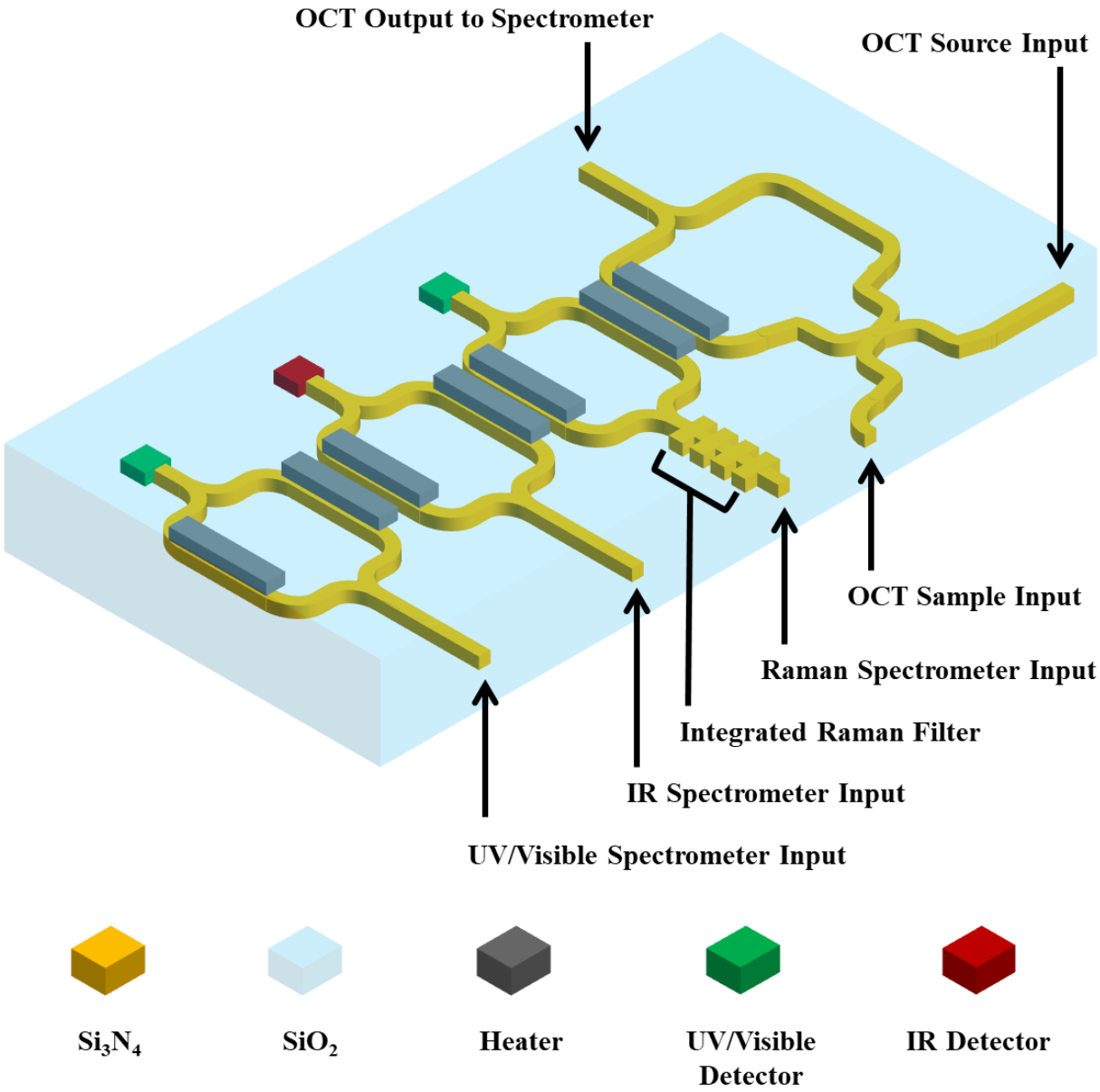

Figure 6.1: Schematic of the proposed multifunctional photonic biosensor chip. Note that the OCT component could either have a dedicated spectrometer, or work in conjunction with the integrated spectrometers. The inputs and outputs will be packaged with standard optical fiber connectors to interface with replaceable fiber sensor collection heads. Not shown are the optical illumination sources. These will be delivered to the sample separately through fiber, although heterogeneous integration onto the biosensor chip is a future possibility.

6.1.2 Sensor technology and design

The proposed multifunctional photonic biosensor is illustrated in Figure 6.1. The optical sensing techniques enabled by the device include: conventional spectroscopy at various wavelength regimes, fluorescence spectroscopy, Raman spectroscopy, and optical coherence tomography [1]. These techniques will all require a spectrometer and source at the relevant wavelength. Raman spectroscopy is in need of additional narrowband filtering components, which can be fulfilled with simple integrated components [105]. Similarly, optical coherence tomography requires a basic interferometer prior to the spectrometer, but this has also been demonstrated in an integrated context [106].

There are many possible spectrometer designs [10], however the most attractive in this context is the Fourier transform spectrometer [10,14,57] for a variety of reasons. Specifically, the design is simple and robust, as the calibration procedure can accommodate random fabrication variations. It is also easy to adapt to extremely broadband operation using adiabatic splitters. The control circuitry is also simple, requiring only a single pixel detector. Finally, the design space is highly versatile. The resolution is proportional to the device length, and therefore the footprint can be reduced for applications that require low resolution. Likewise, for narrowband measurement the measurement speed can also be increased due to the Nyquist sampling criterion requiring fewer sampling points.

Another noninvasive technique that has seen considerable development over the past decade is Optical Coherence Tomography (OCT) [107]. As opposed to spectroscopy, OCT provides cross-sectional information of each sample. For blood glucose sensing, OCT can provide useful data as blood vessels occur in a particular depth range beneath the skin tissue. The depth information can be used to extract glucose content of blood through various data extraction

techniques [108]. Hence, in theory, both OCT and spectrometry can be combined on a single integrated chip to measure the blood glucose with greater accuracy and reliability. Also, both on-chip Fourier Transform spectrometer and OCT are interferometric techniques and both can be realized using similar designs, which simplify the engineering. Spectral domain OCT [109] itself requires a spectrometer which again can be implemented in a dedicated manner, or in conjunction with the other spectrometers on the photonic biosensor.

OCT, like Fourier transform spectroscopy, has limitations due to the Nyquist sampling criterion. Specifically, the axial resolution of a single scan in OCT is inversely proportional to the bandwidth of the light source utilized [109]. We propose a novel technique to ease this restriction by making multiple scans with different phase modulation, and then using multirate signal processing [110,111] to obtain much higher depth resolution images. The enhanced resolution will further improve the SNR of the blood glucose signal.

The sensor's source/receiver interfaces themselves will be fiber optic in nature. The recent proliferation of fiber optic sensor varieties is an important development, as they can readily be integrated into a multifunctional sensor. In addition to the chemical information afforded spectroscopically, these sensors can provide relevant environmental information such as temperature and pressure [112]. They are highly sensitive, robust, flexible, and can provide distributed sensing capability over large scales [113,114]. Additional advantages include resistance to electromagnetic interference, and ease of multiplexing [115]. Furthermore, they are both inexpensive and robust. This means they can withstand cleaning and sterilization or be made replaceable and disposable [112].

Given the absorption coefficient of tissue, the measurements will operate by collecting reflected light in order to maximize signal power [7,116]. The simplest optical collection method

involves packaging a fiber with a lens as a collection aperture and placing it in contact or near contact with the tissue for measurement. In this way the same fiber can be used to deliver illumination to the sample as well as collect the reflected signal, as illustrated in Figure 6.2(a) wavelength multiplexer/demultiplexer could even be used to deliver/collect all of the sources simultaneously. However, more advanced distributed fiber sensors that can collect measurement data over an extended area are also possible. A variety of fiber sensors will be considered, and the best down selected for the final device.

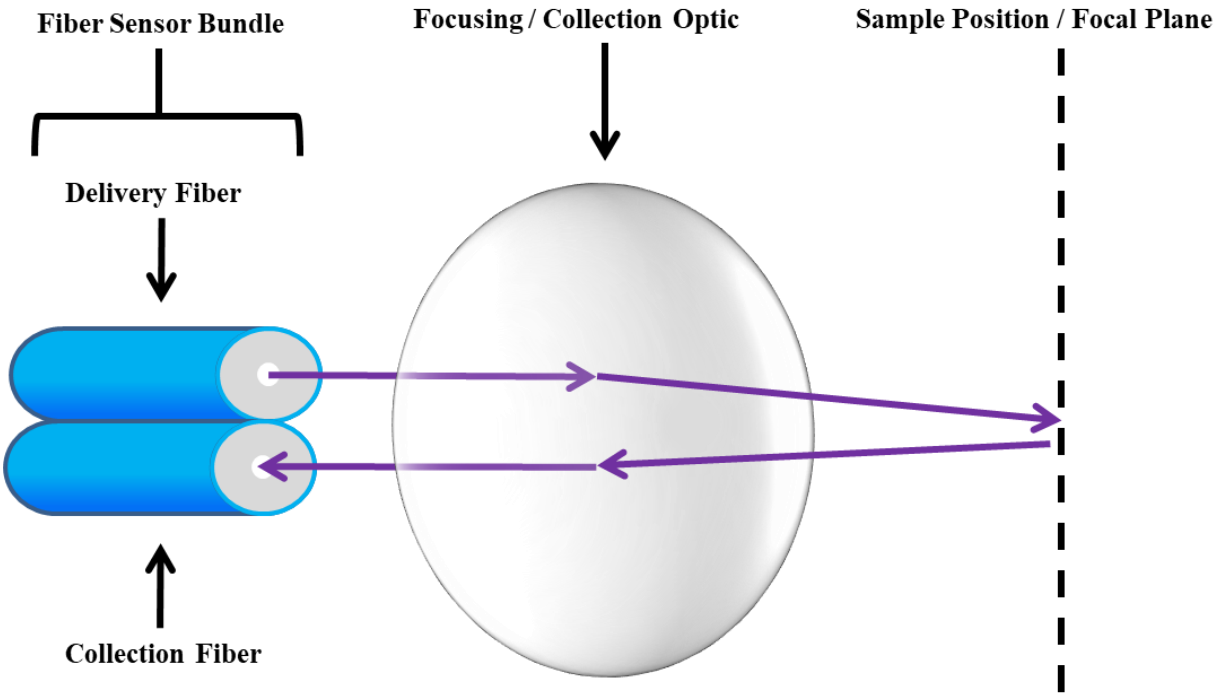

Figure 6.2: Schematic of a fiber sensor head that is configured for simultaneous illumination and signal collection.

6.1.3 Measurements and information fusion

The benefit of using information fusion techniques between multiple optical sensors is well known [8,9]. There is some literature suggesting that linear regression methods outperform nonlinear methods for the spectroscopic characterization of blood glucose level [1]. However, this is limited to a single wavelength regime, and it is not obvious this result will hold in a multi-sensor

regime. Consequently, both linear and nonlinear regression methods should be evaluated in this new context. At the end it's quite essential to simultaneously obtain reference measurements using the conventional glucose meters to compare and evaluate it against the multifunctional photonic biosensor proposed in this work. The results of such device will then be evaluated by Clarke Error Grid analysis, which is the standard method for determining the clinical accuracy of blood glucose meters[1].

6.2 Impacts and future work

The immediate impact of a successful noninvasive glucose sensor will be to "improve diabetic patients' quality of life" (page 2,[1]). More broadly, the device proposed here could form the basis of a truly general multifunctional photonic biosensor. The underlying sensors are already general, as the application space of broadband spectroscopy is nearly universal. The application specific components are the information fusion algorithms, and potentially the fiber sensors. Since the algorithms are performed at the microcontroller level, they are easy to reconfigure on an application-by-application basis. Likewise, the fiber sensors can be easily replaced which makes them simple to customize for different applications. The natural path of future work would be to extend the basic device to other applications by building a library of information fusion algorithms and a selection of fiber sensors. The portable nature of the device would make it easy to network and implement control/monitoring/automation schemes. Furthermore, it would ease measurement standardization. This would be a highly transformative technology.

6.3 Acknowledgment

This chapter uses information from the white paper "Multifunctional Photonic Biosensors with Information Fusion: Blood Glucose Sensing Application Case", Andrew Grieco, Naif Alshamrani, Prabhav Gaur, Karl Johnson, and Yeshaiahu Fainman. The dissertation author was a

co-author in this manuscript and Yeshaiahu Fainman was the principal investigator.

Bibliography

1. R. Zhang, S. Liu, H. Jin, Y. Luo, Z. Zheng, F. Gao, and Y. Zheng, "Noninvasive Electromagnetic Wave Sensing of Glucose," Sensors **19**(5), 1151 (2019).

2. S. K. Vashist, "Non-invasive glucose monitoring technology in diabetes management: A review," Analytica Chimica Acta **750**, 16–27 (2012).

3. J. Yadav, A. Rani, V. Singh, and B. M. Murari, "Prospects and limitations of non-invasive blood glucose monitoring using near-infrared spectroscopy," Biomedical Signal Processing and Control **18**, 214–227 (2015).

4. C. Chen, X.-L. Zhao, Z.-H. Li, Z.-G. Zhu, S.-H. Qian, and A. Flewitt, "Current and Emerging Technology for Continuous Glucose Monitoring," Sensors **17**(1), 182 (2017).

5. D. Bruen, C. Delaney, L. Florea, and D. Diamond, "Glucose Sensing for Diabetes Monitoring: Recent Developments," Sensors **17**(8), 1866 (2017).

6. L. Tang, S. J. Chang, C.-J. Chen, and J.-T. Liu, "Non-Invasive Blood Glucose Monitoring Technology: A Review," Sensors **20**(23), 6925 (2020).

7. B. Alsunaidi, M. Althobaiti, M. Tamal, W. Albaker, and I. Al-Naib, "A Review of Non-Invasive Optical Systems for Continuous Blood Glucose Monitoring," Sensors **21**(20), 6820 (2021).

8. L. Rolinger, M. Rüdt, and J. Hubbuch, "A critical review of recent trends, and a future perspective of optical spectroscopy as PAT in biopharmaceutical downstream processing," Analytical and Bioanalytical Chemistry **412**(9), 2047–2064 (2020).

9. C. Pasquini, "Near infrared spectroscopy: A mature analytical technique with new perspectives – A review," Analytica Chimica Acta **1026**, 8–36 (2018).

10. Z. Yang, T. Albrow-Owen, W. Cai, and T. Hasan, "Miniaturization of optical spectrometers," Science (1979) **371**(6528), eabe0722 (2021).

11. N. Alshamrani, A. Grieco, A. Friedman, K. A. Johnson, M.-S. Kim, F. Floris, P. O'brien, and Y. Fainman, "A Non-Mechanical Multi-Wavelength Integrated Photonic Beam Steering System," Journal of Lightwave Technology **39**(12), 4201–4208 (2021).

12. N. Alshamrani, A. Grieco, B. Hong, and Y. Fainman, "Miniaturized integrated spectrometer using a silicon ring-grating design," Optics Express **29**(10), 15279–15287 (2021).

13. S. Kumar, N. Alshamrani, A. Grieco, and Y. Fainman, "Side-lobe reduction by cascading Bragg grating filters on a Si-photonic chip," Optics Express **30**(6), 9983–9991 (2022).

14. A. Li, J. Davis, A. Grieco, N. Alshamrani, and Y. Fainman, "Fabrication-tolerant Fourier transform spectrometer on silicon with broad bandwidth and high resolution," Photonics Research **8**(2), 219–224 (2020).

15. P. F. McManamon and A. Ataei, "Progress and opportunities in optical beam steering," in *Quantum Sensing and Nano Electronics and Photonics XVI* (SPIE, 2019), p. 1092610.

16. M. C. Wu, L.-Y. Lin, S.-S. Lee, and K. S. J. Pister, "Micromachined free-space integrated micro-optics," Sensors and Actuators A: Physical **50**(1–2), 127–134 (1995).

17. O. Solgaard, "Miniaturization of free space optical systems," Applied Optics **49**(25), F18 (2010).

18. S. Shaoxin, R. Xuechang, L. Shou, Y. Zhilin, and Z. Yuanying, "Fabrication of large-scale photonic phased array using a holographic lithography system," Optical Engineering **52**(9), 095103 (2013).

19. J. Sun, E. Timurdogan, A. Yaacobi, Zhan Su, E. S. Hosseini, D. B. Cole, and M. R. Watts, "Large-Scale Silicon Photonic Circuits for Optical Phased Arrays," IEEE Journal of Selected Topics in Quantum Electronics **20**(4), 264–278 (2014).

20. P. F. McManamon, T. A. Dorschner, D. L. Corkum, L. J. Friedman, D. S. Hobbs, M. Holz, S. Liberman, H. Q. Nguyen, D. P. Resler, R. C. Sharp, and E. A. Watson, "Optical phased array technology," Proceedings of the IEEE **84**(2), 268–298 (1996).

21. F. Ashtiani and F. Aflatouni, "N × N optical phased array with 2N phase shifters," Optics Express **27**(19), 27183 (2019).

22. J. Sun, E. Timurdogan, A. Yaacobi, E. S. Hosseini, and M. R. Watts, "Large-scale nanophotonic phased array," Nature **493**(7431), 195–199 (2013).

23. K. van Acoleyen, K. Komorowska, W. Bogaerts, and R. Baets, "One-Dimensional Off-Chip Beam Steering and Shaping Using Optical Phased Arrays on Silicon-on-Insulator," Journal of Lightwave Technology **29**(23), 3500–3505 (2011).

24. A. GRIECO, A. E L AMILI, Y. FAINMAN, and S. PAPPERT, *"Photonic Beam Steering and Applications for Optical Communications," U.S. Provisional. Ser. No. 62/651,025, Filed Mar. 2018.* (2018).

25. D. Inoue, T. Ichikawa, A. Kawasaki, and T. Yamashita, "Demonstration of a new optical scanner using silicon photonics integrated circuit," Optics Express **27**(3), 2499 (2019).

26. C. Li, X. Cao, K. Wu, X. Li, and J. Chen, "Lens-based integrated 2D beam-steering device with defocusing approach and broadband pulse operation for Lidar application," Optics Express **27**(23), 32970 (2019).

27. W. Rotman and R. Turner, "Wide-angle microwave lens for line source applications," IEEE Transactions on Antennas and Propagation **11**(6), 623–632 (1963).

28. J. W. Goodman, *Introduction to Fourier Optics*, 3rd ed (Roberts & Co., 2005).

29. T. Čižmár, V. Kollárová, X. Tsampoula, F. Gunn-Moore, W. Sibbett, Z. Bouchal, and K. Dholakia, "Generation of multiple Bessel beams for a biophotonics workstation," Optics Express **16**(18), 14024 (2008).

30. "NanoSOI Fabrication Service | Applied Nanotools Inc.," Available at: https://www.appliednt.com/.

31. K. Ikeda, K. Suzuki, R. Konoike, S. Namiki, and H. Kawashima, "Large-scale silicon photonics switch based on 45-nm CMOS technology," Optics Communications **466**, 125677 (2020).

32. D. Nikolova, S. Rumley, D. Calhoun, Q. Li, R. Hendry, P. Samadi, and K. Bergman, "Scaling silicon photonic switch fabrics for data center interconnection networks," Optics Express **23**(2), 1159–1175 (2015).

33. A. Biberman, G. Hendry, J. Chan, H. Wang, K. Bergman, K. Preston, N. Sherwood-Droz, J. S. Levy, and M. Lipson, "CMOS-compatible scalable photonic switch architecture using 3D-integrated deposited silicon materials for high-performance data center networks," in *2011 Optical Fiber Communication Conference and Exposition and the National Fiber Optic Engineers Conference* (OSA, 2011), pp. 1–3.

34. M. Bahadori, M. Nikdast, S. Rumley, L. Y. Dai, N. Janosik, T. van Vaerenbergh, A. Gazman, Q. Cheng, R. Polster, and K. Bergman, "Design Space Exploration of Microring Resonators in Silicon Photonic Interconnects: Impact of the Ring Curvature," Journal of Lightwave Technology **36**(13), 2767–2782 (2018).

35. J. R. Ong, R. Kumar, and S. Mookherjea, "Ultra-High-Contrast and Tunable-Bandwidth Filter Using Cascaded High-Order Silicon Microring Filters," IEEE Photonics Technology Letters **25**(16), 1543–1546 (2013).

36. L. Carroll, *Silicon Photonics Packaging Services for EuroPractice-MPW Runs* (2016).

37. L. Chrostowski, Z. Lu, J. Flueckiger, X. Wang, J. Klein, A. Liu, J. Jhoja, and J. Pond, "Design and simulation of silicon photonic schematics and layouts," in *Silicon Photonics and Photonic Integrated Circuits V* (SPIE, 2016), **9891**, p. 989114.

38. L. Chrostowski and M. Hochberg, *Silicon Photonics Design* (Cambridge University Press, 2015).

39. W. Bogaerts, P. de Heyn, T. van Vaerenbergh, K. de Vos, S. Kumar Selvaraja, T. Claes, P. Dumon, P. Bienstman, D. van Thourhout, and R. Baets, "Silicon microring resonators," Laser & Photonics Reviews **6**(1), 47–73 (2012).

40. M. Geng, L. Jia, L. Zhang, L. Yang, P. Chen, T. Wang, and Y. Liu, "Four-channel reconfigurable optical add-drop multiplexer based on photonic wire waveguide," Optics Express **17**(7), 5502 (2009).

41. P. Dong, W. Qian, H. Liang, R. Shafiiha, N.-N. Feng, D. Feng, X. Zheng, A. v. Krishnamoorthy, and M. Asghari, "Low power and compact reconfigurable multiplexing devices based on silicon microring resonators," Optics Express **18**(10), 9852 (2010).

42. J. Bachman, "Factory acceptance test," Applied Nano tools Inc., Edmonton, Alberta, Canada, 2020. [Online]. Available: jocelyn@appliednt.com (2020).

43. K. Suzuki, R. Konoike, J. Hasegawa, S. Suda, H. Matsuura, K. Ikeda, S. Namiki, and H. Kawashima, "Low-Insertion-Loss and Power-Efficient 32 × 32 Silicon Photonics Switch With Extremely High-Δ Silica PLC Connector," Journal of Lightwave Technology **37**(1), 116–122 (2019).

44. D. Munk, M. Katzman, Y. Kaganovskii, N. Inbar, A. Misra, M. Hen, M. Priel, M. Feldberg, M. Tkachev, A. Bergman, M. Vofsi, M. Rosenbluh, T. Schneider, and A. Zadok, "Eight-Channel Silicon-Photonic Wavelength Division Multiplexer With 17 GHz Spacing," IEEE Journal of Selected Topics in Quantum Electronics **25**(5), 1–10 (2019).

45. D. Munk, M. Katzman, M. Hen, M. Priel, A. Bergman, A. Zadok, Y. Kaganovskii, M. Rosenbluh, N. Inbar, and M. Vofsy, "Silicon-Photonic Dense 8-Channel Multiplexer Using Auto-Regressive Moving-Average Filters," in *2018 International Topical Meeting on Microwave Photonics (MWP)* (IEEE, 2018), pp. 1–4.

46. S. Chung, M. Nakai, E. Preisler, and H. Hashemi, "Poly-Crystalline Silicon Waveguide Devices on Hollow Deep Trench Isolation in Standard Foundry Bulk Silicon Process," in *2018 Optical Fiber Communications Conference and Exposition (OFC)* (2018), pp. 1–3.

47. T. Aalto, M. Cherchi, M. Harjanne, S. Bhat, P. Heimala, F. Sun, M. Kapulainen, T. Hassinen, and T. Vehmas, "Open-Access 3-μm SOI Waveguide Platform for Dense Photonic Integrated Circuits," IEEE Journal of Selected Topics in Quantum Electronics **25**(5), 1–9 (2019).

48. S. W. Kim, K. J. Yee, M. Abashin, L. Pang, and Y. Fainman, "Composite dielectric metasurfaces for phase control of vector field," Optics Letters **40**(11), 2453 (2015).

49. Y. Masumoto and T. Takagahara, *Semiconductor Quantum Dots*, NanoScience and Technology (Springer Berlin Heidelberg, 2002).

50. K. Kochan, E. Lai, Z. Richardson, C. Nethercott, A. Y. Peleg, P. Heraud, and B. R. Wood, "Vibrational Spectroscopy as a Sensitive Probe for the Chemistry of Intra-Phase Bacterial Growth," Sensors **20**(12), 3452 (2020).

51. S. Guo, P. Rösch, J. Popp, and T. Bocklitz, "Modified PCA and PLS: Towards a better classification in Raman spectroscopy–based biological applications," Journal of Chemometrics **34**(4), e3202 (2020).

52. M. Ferrari and V. Quaresima, "A brief review on the history of human functional near-infrared spectroscopy (fNIRS) development and fields of application," Neuroimage **63**(2), 921–935 (2012).

53. W. F. X. Frank and W. Goertz, "Measurement of transmission properties of optical fibers for telecommunications by FT-IR spectroscopy," Mikrochimica Acta **94**(1–6), 309–314 (1988).

54. A. Z. Subramanian, E. Ryckeboer, A. Dhakal, F. Peyskens, A. Malik, B. Kuyken, H. Zhao, S. Pathak, A. Ruocco, A. de Groote, P. Wuytens, D. Martens, F. Leo, W. Xie, U. D. Dave, M. Muneeb, P. van Dorpe, J. van Campenhout, W. Bogaerts, P. Bienstman, N. le Thomas, D. van Thourhout, Z. Hens, G. Roelkens, and R. Baets, "Silicon and silicon nitride photonic circuits for spectroscopic sensing on-a-chip [Invited]," Photonics Research **3**(5), B47–B59 (2015).

55. K. B. Beć and C. W. Huck, "Breakthrough Potential in Near-Infrared Spectroscopy: Spectra Simulation. A Review of Recent Developments," Frontiers in Chemistry **7**, 48 (2019).

56. M. Vainio and L. Halonen, "Mid-infrared optical parametric oscillators and frequency combs for molecular spectroscopy," Physical Chemistry Chemical Physics **18**(6), 4266–4294 (2016).

57. M. C. M. M. Souza, A. Grieco, N. C. Frateschi, and Y. Fainman, "Fourier transform spectrometer on silicon with thermo-optic non-linearity and dispersion correction," Nature Communications **9**(1), 665 (2018).

58. X. Ma, M. Li, and J.-J. He, "CMOS-Compatible Integrated Spectrometer Based on Echelle Diffraction Grating and MSM Photodetector Array," IEEE Photonics Journal **5**(2), 6600807 (2013).

59. M. Nedeljkovic, A. v. Velasco, A. Z. Khokhar, A. Delage, P. Cheben, and G. Z. Mashanovich, "Mid-Infrared Silicon-on-Insulator Fourier-Transform Spectrometer Chip," IEEE Photonics Technology Letters **28**(4), 528–531 (2016).

60. M. Florjańczyk, P. Cheben, S. Janz, B. Lamontagne, J. Lapointe, A. Scott, B. Solheim, and D.-X. Xu, "Development of a slab waveguide spatial heterodyne spectrometer for remote sensing," in *MOEMS and Miniaturized Systems IX* (SPIE, 2010), **7594**, p. 75940R.

61. M. Erfan, Y. M. Sabry, M. Sakr, B. Mortada, M. Medhat, and D. Khalil, "On-Chip Micro–Electro–Mechanical System Fourier Transform Infrared (MEMS FT-IR) Spectrometer-Based Gas Sensing," Applied Spectroscopy **70**(5), 897–904 (2016).

62. B. HONG, Y. FAINMAN, and A. GRIECO, *Miniaturized and Integrated Photonic Spectrometers. US Patent App. 16/303,653.* (2020).

63. K. Ikeda, M. Nezhad, and Y. Fainman, "Wavelength selective coupler with vertical gratings on silicon chip," Applied Physics Letters **92**(20), 201111 (2008).

64. J. A. Davis, A. Li, N. Alshamrani, and Y. Fainman, "Silicon photonic chip for 16-channel wavelength division (de-)multiplexing in the O-band," Opt Express **28**(16), 23620–23627 (2020).

65. A. Grieco, B. Slutsky, D. T. H. Tan, S. Zamek, M. P. Nezhad, and Y. Fainman, "Optical Bistability in a Silicon Waveguide Distributed Bragg Reflector Fabry–Pérot Resonator," Journal of Lightwave Technology **30**(14), 2352–2355 (2012).

66. P. Sun and R. M. Reano, "Low-power optical bistability in a free-standing silicon ring resonator," Optics Letters **35**(8), 1124–1126 (2010).

67. A. Grieco, B. Slutsky, and Y. Fainman, "Characterization of waveguide loss using distributed Bragg reflectors," Applied Physics B **114**(4), 467–474 (2014).

68. A. Grieco and Y. Fainman, "Characterization of Distributed Bragg Reflectors," IEEE Journal of Quantum Electronics **50**(6), 453–457 (2014).

69. S. Sedky, A. Witvrouw, H. Bender, and K. Baert, "Experimental determination of the maximum post-process annealing temperature for standard CMOS wafers," IEEE Transactions on Electron Devices **48**(2), 377–385 (2001).

70. W. Shi, X. Wang, C. Lin, H. Yun, Y. Liu, T. Baehr-Jones, M. Hochberg, N. A. F. Jaeger, and L. Chrostowski, "Silicon photonic grating-assisted, contra-directional couplers," Optics Express **21**(3), 3633–3650 (2013).

71. C. K. Madsen and J. H. Zhao, *Optical Filter Design and Analysis: A Signal Processing Approach* (Wiley-Interscience, 1999).

72. D. Charron and W. Shi, "O-band add-drop filter in Bragg-grating-assisted Mach-Zehnder interferometers for CWDM," in *Conference on Lasers and Electro-Optics* (OSA, 2019), p. JTh2A.44.

73. Y. S. Fainman, J. Ford, W. M. Mellette, S. Mookherjea, G. Porter, A. C. Snoeren, G. Papen, S. Saeedi, J. Cunningham, A. Krishnamoorthy, M. Gehl, C. T. DeRose, P. S. Davids, D. C. Trotter, A. L. Starbuck, C. M. Dallo, D. Hood, A. Pomerene, and A. Lentine, "LEED: A Lightwave Energy-Efficient Datacenter," in *2019 Optical Fiber Communications Conference and Exhibition (OFC)* (OSA, 2019), pp. 1–3.

74. H. Qiu, J. Jiang, P. Yu, D. Mu, J. Yang, X. Jiang, H. Yu, R. Cheng, and L. Chrostowski, "Narrow-Band Add-Drop Filter Based on Phase-Modulated Grating-Assisted Contra-Directional Couplers," Journal of Lightwave Technology **36**(17), 3760–3764 (2018).

75. X. Zhao, Y. Wang, Q. Huang, and J. Xia, "Two-mode contra-directional coupler based on superposed grating," Optics Express **25**(3), 2654–2665 (2017).

76. J. St-Yves, H. Bahrami, P. Jean, S. LaRochelle, and W. Shi, "Widely bandwidth-tunable silicon filter with an unlimited free-spectral range," Optics Letters **40**(23), 5471–5474 (2015).

77. A. D. Simard, N. Belhadj, Y. Painchaud, and S. LaRochelle, "Apodized Silicon-on-Insulator Bragg Gratings," IEEE Photonics Technology Letters **24**(12), 1033–1035 (2012).

78. D. T. H. Tan, K. Ikeda, S. Zamek, A. Mizrahi, M. Nezhad, A. V. Krishnamoorthy, K. Raj, J. E. Cunningham, X. Zheng, I. Shubin, Y. Luo, and Y. Fainman, "Wide Bandwidth, Low Loss 1 by 4 Wavelength Division Multiplexer on Silicon for Optical Interconnects," in *Optical Fiber Communication Conference/National Fiber Optic Engineers Conference 2011* (OSA, 2011), **19**(3), p. OMM4.

79. H. Yun, M. Hammood, S. Lin, L. Chrostowski, and N. A. F. Jaeger, "Broadband flat-top SOI add–drop filters using apodized sub-wavelength grating contradirectional couplers," Optics Letters **44**(20), 4929–4932 (2019).

80. P. S. Cross and H. Kogelnik, "Sidelobe suppression in corrugated-waveguide filters," Optics Letters **1**(1), 43–45 (1977).

81. A. Karimi, F. Emami, and N. Nozhat, "The effects of various apodization functions on the filtering characteristics of the grating-assisted SOI strip waveguides," J Opt Soc Korea **18**(2), 101–109 (2014).

82. S. Kumar, "Design and Manipulation of On-Chip Bragg Couplers for Side Lobe Suppression," University of California, San Diego (2018).

83. A. Yariv and P. Yeh, *Optical Waves in Crystals : Propagation and Control of Laser Radiation* (Hoboken, N.J. : Wiley-Interscience, 2003).

84. J.-P. Weber, "Spectral characteristics of coupled-waveguide Bragg-reflection tunable optical filter," IEE Proceedings J Optoelectronics **140**(5), 275–284 (1993).

85. D. I. Ellis, D. Broadhurst, D. B. Kell, J. J. Rowland, and R. Goodacre, "Rapid and Quantitative Detection of the Microbial Spoilage of Meat by Fourier Transform Infrared Spectroscopy and Machine Learning," Applied and Environmental Microbiology **68**(6), 2822–2828 (2002).

86. C. Pacholski, M. Sartor, M. J. Sailor, F. Cunin, and G. M. Miskelly, "Biosensing Using Porous Silicon Double-Layer Interferometers: Reflective Interferometric Fourier Transform Spectroscopy," J Am Chem Soc **127**(33), 11636–11645 (2005).

87. E. le Coarer, S. Blaize, P. Benech, I. Stefanon, A. Morand, G. Lérondel, G. Leblond, P. Kern, J. M. Fedeli, and P. Royer, "Wavelength-scale stationary-wave integrated Fourier-transform spectrometry," Nature Photonics **1**(8), 473–478 (2007).

88. P. B. Fellgett, "On the Ultimate Sensitivity and Practical Performance of Radiation Detectors," J Opt Soc Am **39**(11), 970–976 (1949).

89. A. E.-J. Lim, J. Song, Q. Fang, C. Li, X. Tu, N. Duan, K. K. Chen, R. P.-C. Tern, and T.-Y. Liow, "Review of Silicon Photonics Foundry Efforts," IEEE Journal of Selected Topics in Quantum Electronics **20**(4), 405–416 (2014).

90. A. v. Velasco, P. Cheben, P. J. Bock, A. Delâge, J. H. Schmid, J. Lapointe, S. Janz, M. L. Calvo, D.-X. Xu, M. Florjańczyk, and M. Vachon, "High-resolution Fourier-transform

spectrometer chip with microphotonic silicon spiral waveguides," Optics Letters **38**(5), 706–708 (2013).

91. B. I. Akca, "Design of a compact and ultrahigh-resolution Fourier-transform spectrometer," Optics Express **25**(2), 1487–1494 (2017).

92. H. Podmore, A. Scott, P. Cheben, A. v. Velasco, J. H. Schmid, M. Vachon, and R. Lee, "Demonstration of a compressive-sensing Fourier-transform on-chip spectrometer," Optics Letters **42**(7), 1440–1443 (2017).

93. X. Nie, E. Ryckeboer, G. Roelkens, and R. Baets, "CMOS-compatible broadband co-propagative stationary Fourier transform spectrometer integrated on a silicon nitride photonics platform," Optics Express **25**(8), A409–A418 (2017).

94. S. N. Zheng, J. Zou, H. Cai, J. F. Song, L. K. Chin, P. Y. Liu, Z. P. Lin, D. L. Kwong, and A. Q. Liu, "Microring resonator-assisted Fourier transform spectrometer with enhanced resolution and large bandwidth in single chip solution," Nature Communications **10**(1), 2349 (2019).

95. M.-C. Tien, J. F. Bauters, M. J. R. Heck, D. T. Spencer, D. J. Blumenthal, and J. E. Bowers, "Ultra-high quality factor planar Si3N4 ring resonators on Si substrates," Optics Express **19**(14), 13551–13556 (2011).

96. H. Qiu, F. Zhou, J. Qie, Y. Yao, X. Hu, Y. Zhang, X. Xiao, Y. Yu, J. Dong, and X. Zhang, "A Continuously Tunable Sub-Gigahertz Microwave Photonic Bandpass Filter Based on an Ultra-High-Q Silicon Microring Resonator," Journal of Lightwave Technology **36**(19), 4312–4318 (2018).

97. D. M. Kita, B. Miranda, D. Favela, D. Bono, J. Michon, H. Lin, T. Gu, and J. Hu, "High-performance and scalable on-chip digital Fourier transform spectroscopy," Nature Communications **9**(1), 4405 (2018).

98. W. Bogaerts, R. Baets, P. Dumon, V. Wiaux, S. Beckx, D. Taillaert, B. Luyssaert, J. van Campenhout, P. Bienstman, and D. van Thourhout, "Nanophotonic waveguides in silicon-on-insulator fabricated with CMOS technology," Journal of Lightwave Technology **23**(1), 401–412 (2005).

99. A. Li, T. van Vaerenbergh, P. de Heyn, P. Bienstman, and W. Bogaerts, "Backscattering in silicon microring resonators: a quantitative analysis," Laser & Photonics Reviews **10**(3), 420–431 (2016).

100. A. Li, Y. Xing, R. van Laer, R. Baets, and W. Bogaerts, "Extreme spectral transmission fluctuations in silicon nanowires induced by backscattering," in *2016 IEEE 13th International Conference on Group IV Photonics (GFP)* (IEEE, 2016), **2016-November**, pp. 160–161.

101. S. K. Selvaraja, W. Bogaerts, and D. van Thourhout, "Loss reduction in silicon nanophotonic waveguide micro-bends through etch profile improvement," Optics Communications **284**(8), 2141–2144 (2011).

102. Z. Lu, J. Jhoja, J. Klein, X. Wang, A. Liu, J. Flueckiger, J. Pond, and L. Chrostowski, "Performance prediction for silicon photonics integrated circuits with layout-dependent correlated manufacturing variability," Optics Express **25**(9), 9712–9733 (2017).

103. H. Lin, Z. Luo, T. Gu, L. C. Kimerling, K. Wada, A. Agarwal, and J. Hu, "Mid-infrared integrated photonics on silicon: a perspective," Nanophotonics **7**(2), 393–420 (2018).

104. P. Munoz, P. W. L. van Dijk, D. Geuzebroek, M. Geiselmann, C. Dominguez, A. Stassen, J. D. Domenech, M. Zervas, A. Leinse, C. G. H. Roeloffzen, B. Gargallo, R. Banos, J. Fernandez, G. M. Cabanes, L. A. Bru, and D. Pastor, "Foundry Developments Toward Silicon Nitride Photonics From Visible to the Mid-Infrared," IEEE Journal of Selected Topics in Quantum Electronics **25**(5), 1–13 (2019).

105. D. T. H. Tan, K. Ikeda, and Y. Fainman, "Cladding-modulated Bragg gratings in silicon waveguides," Optics Letters **34**(9), 1357–1359 (2009).

106. S. Schneider, M. Lauermann, P.-I. Dietrich, C. Weimann, W. Freude, and C. Koos, "Optical coherence tomography system mass-producible on a silicon photonic chip," Optics Express **24**(2), 1573–1586 (2016).

107. A. C. S. Tan, G. S. Tan, A. K. Denniston, P. A. Keane, M. Ang, D. Milea, U. Chakravarthy, and C. M. G. Cheung, "An overview of the clinical applications of optical coherence tomography angiography," Eye **32**(2), 262–286 (2018).

108. L. R. de Pretto, T. M. Yoshimura, M. S. Ribeiro, and A. Zanardi de Freitas, "Optical coherence tomography for blood glucose monitoring *in vitro* through spatial and temporal approaches," Journal of Biomedical Optics **21**(8), 086007 (2016).

109. S. Aumann, S. Donner, J. Fischer, and F. Müller, "Optical Coherence Tomography (OCT): Principle and Technical Realization," in *High Resolution Imaging in Microscopy and Ophthalmology: New Frontiers in Biomedical Optics*, J. F. Bille, ed. (Springer International Publishing, 2019).

110. J. R. Zuluaga and J. L. Naredo, "Poly-phase filter-bank realization for the simulation of electric-network transients," in *2014 11th International Conference on Electrical Engineering, Computing Science and Automatic Control (CCE)* (IEEE, 2014), pp. 1–6.

111. P. Gaur, A. Grieco, N. Alshamrani, D. Almutairi, and Y. Fainman, "Universal photonics tomography," Optics Express **30**(11), 19222–19235 (2022).

112. C. Dincer, R. Bruch, E. Costa-Rama, M. T. Fernández-Abedul, A. Merkoçi, A. Manz, G. A. Urban, and F. Güder, "Disposable Sensors in Diagnostics, Food, and Environmental Monitoring," Advanced Materials **31**(30), 1806739 (2019).

113. X. Lu, P. J. Thomas, and J. O. Hellevang, "A Review of Methods for Fibre-Optic Distributed Chemical Sensing," Sensors **19**(13), 2876 (2019).

114. A. G. Leal-Junior, C. A. R. Diaz, L. M. Avellar, M. J. Pontes, C. Marques, and A. Frizera, "Polymer Optical Fiber Sensors in Healthcare Applications: A Comprehensive Review," Sensors **19**(14), 3156 (2019).

115. S. Pevec and D. Donlagić, "Multiparameter fiber-optic sensors: a review," Optical Engineering **58**(7), 072009 (2019).

116. E. Hemmer, A. Benayas, F. Légaré, and F. Vetrone, "Exploiting the biological windows: current perspectives on fluorescent bioprobes emitting above 1000 nm," Nanoscale Horizons **1**(3), 168–184 (2016).